Bull. Mar. Sci & Tech 11(1), 2002
Research Institute of Marine Science and Technology
Korea Maritime University

A three-dimensional mixed finite-difference Galerkin function model for the oceanic circulation in the Yellow Sea and the East China Sea in the presence of M_2 tide

Ho Jin Lee[a], Kyung Tae Jung[a,*], Jae Kwi So[a], Jong Yul Chung[b]

[a] *Korea Ocean Research and Development Institute, Ansan P.O. Box 29, Seoul 425-600, South Korea*
[b] *Department of Oceanography, Seoul National University, Seoul 151-742, South Korea*

Received 23 April 1999; received in revised form 14 November 2000; accepted 23 May 2001

Abstract

This paper, as a sequel to Lee et al. (Continental Shelf Research 20 (2000) 863) describes the simulation of the oceanic current in the Yellow Sea (YS) and the East China Sea (ECS) with forcings of M_2 tide as well as oceanic flows prescribed at the open boundary. The model is three dimensional and barotropic, and uses a finite-difference approximation in the horizontal plane and function expansions in the vertical direction. The bottom stress is represented by the conventional quadratic friction law and the vertical eddy viscosity takes a flow-related form. A radiation condition is employed along the open boundaries to handle the M_2 tide and oceanic flows simultaneously.

From a series of numerical calculations with M_2 tide forcing only, the bottom friction coefficient, 0.0035, has been found as an optimum value with which RMS errors (amplitude, phase lag) are calculated as 16.4 cm, 19.5°. Calculations have also been carried out to investigate the effects of using an empirical function expansion for the current profiles below the main stream of Kuroshio. Despite the bias of the tidal propagation and the associated flux, the tidal chart has been calculated with tolerable accuracy. The model calculation confirms the results of Exp. 4 of Lee et al. (Continental Shelf Research 20 (2000) 863), in that the tide-enhanced bottom friction effectively blocks the penetration of northwestward flow into the YS known as the Yellow Sea Warm Current (YSWC). The presence of small gyres, however, complicates the circulation near the southern YS and west of Cheju Island and tidal residual currents omnipresent at the shallow sea region off the Chinese coast between 32°N and 34.5°N also contribute to the suppression of the formation of the YSWC. The distribution of the sea surface elevation averaged over the M_2 tidal period is qualitatively in good agreement with that of Yanagi et al. (Continental Shelf Research 17 (1997) 655), calculated from the TOPEX altimetric data. Calculation with an inflow of 25.1 Sv through open boundaries on both sides of Taiwan shows that 1.15 Sv goes through Korea/Tsushima Strait, 0.36 Sv through the north of Tokara Strait (between Kyushu and Yakushima Island), 20.95 Sv through Tokara Strait and 2.77 Sv through open boundaries along the Ryukyu Islands. Calculations with fortnightly variation in M_2 open boundary forcings show that the oceanic circulation as well as tidal residuals vary significantly in the southern Yellow Sea; penetration of oceanic flows into the Yellow Sea occurs deeper at the neap tide than at the spring tide. The seasonal variation in the volume transport of the oceanic inflows/outflows without baroclinic effects has little effect on the exchange between the YS and the ECS.

Keywords: Yellow Sea; East China Sea; Oceanic circulation; M_2 tide

*Corresponding author.

1. Introduction

This paper, as a sequel to Lee et al. (2000), deals with an application of a three-dimensional hydrodynamic numerical model to the Yellow Sea (YS) and the East China Sea (ECS) to simulate the dynamic behavior of oceanic current in the presence of M_2 tide. In the previous study the M_2 tidal current, which constitutes the primary circulation in the YS and in a considerable part of the ECS, indirectly participated in the solution procedure; the motion was then driven by oceanic inflows and outflows prescribed at the open boundaries through a radiational condition based on Flather (1976); the amplitudes of the M_2 tidal current computed in the absence of oceanic current were used to give enhanced estimates of the bottom frictional coefficient and the vertical eddy viscosity coefficient; the formulation of Hunter (1975) was used to modify the bottom frictional coefficient, and the background turbulence induced by the M_2 tidal current was taken into account in defining the vertical eddy viscosity by extending the formulation of Davies and Aldridge (1993). The salient feature of the model used was that the oceanic current was simulated on a homogeneous framework, that is, by solving the three-dimensional, time-dependent, fully nonlinear hydrodynamic equations of motion under hydrostatic balance. To incorporate a stratified behavior of the oceanic flow, that is, the trapping of the main stream in the surface layer of about 300 m thickness, an empirical function was introduced to represent the current profile below the surface layer. The model determines the temporal and spatial variation of sea surface elevation and three components of current using the finite-difference method in the horizontal direction and a Galerkin function method. The aim of the paper was to investigate the effects of M_2 tidal currents on the oceanic circulation in the southern part of the YS and in the ECS. Two cases were compared. One is a calculation of the oceanic flow using the conventional representation of bottom friction, that is, a quadratic bottom friction law with a time- and space-invariant coefficient (0.0025), another is the calculation of the oceanic flows using a linearized bottom friction law the coefficient of which is time- and space-dependent according to the variation in the amplitudes of the background M_2 tidal flows. The model satisfactorily simulated the pattern of the Kuroshio main stream, and reproduced interesting features of the oceanic flows in shelf seas, showing excellent agreement with the ARGOS drifting buoy results by Lie and Cho (1997). One of the important conclusions was that the enhanced bottom friction induced by strong tidal stirring effectively blocks the intrusion of the oceanic flow into the YS known as the Yellow Sea Warm Current (YSWC).

In this paper the simulation of the oceanic flow in the same area is repeated. The obvious difference of the study from Lee et al. (2000) is that the model is forced by the M_2 tide as well as oceanic flows prescribed at the open boundary. For that, we further extend the radiational condition. Hunter's linearization procedure of the quadratic bottom friction law and the parameterization of the vertical eddy viscosity using the information on tidal amplitudes known a priori which take into account the mixing of the primary circulation is no longer used. To the knowledge of the authors, there has been no attempt to model tides and oceanic current simultaneously in a macro-tidal region. Numerical modeling of the oceanic circulation is quite well developed but most attention has been paid to the modeling of the individual processes, neglecting the dynamic interaction between processes; for the cases of modeling multiple processes a clamped condition is frequently used. It is hardly expected that use of a clamped open boundary condition in multiple processes modeling can give an accurate reproduction of the processes involved and their interaction. The use of a radiational condition is prerequisite to the multiple process modeling. The direct calculations of the M_2 tide and the oceanic flows admit nonlinear interactions in more versatile ways through the advection and bottom friction terms in the momentum equations and the shallow water term in the continuity equation. The present study is indeed a first step in the modeling of multiple processes in the YS and ECS although our immediate concern is to confirm the results of Lee et al. (2000).

We initially carry out a series of model runs for a range of input parameters such as the thickness of the Kuroshio main stream and the bottom frictional coefficient. The model results are compared with observations of tidal elevation and current. Once the tide is calibrated, main model runs are carried out with additional oceanic inflow and outflow open boundary forcings at the open boundaries to investigate the behavior of the oceanic flow in the shelf seas. In that course, we intend to confirm the results from Exp. 4 of Lee et al. (2000), that is, the tide-enhanced bottom friction blocks the penetration of the oceanic current into the YS. The distribution of mean sea surface elevation is compared with the sea surface dynamic topography estimated from the altimetric data of Yanagi et al. (1997). Finally, we examine the effects of spring–neap modulation of tide and the seasonal variation in oceanic inflows/outflows, comparing fluxes at a cross section at the southern YS area.

2. The model

2.1. Basic equations and their solutions in terms of function expansion in the vertical direction

We consider a homogenous water under hydrostatic pressure. The three-dimensional, nonlinear, time-dependent, free surface, primitive equations of motion on spherical coordinates are

$$\frac{\partial \xi}{\partial t}+\frac{1}{R\cos\phi}\frac{\partial}{\partial \lambda}\left\{\int_{-\xi}^{h} u\,dz\right\} +\frac{1}{R\cos\phi}\frac{\partial}{\partial \phi}\left\{\int_{-\xi}^{h} v\cos\phi\,dz\right\}=0, \tag{1}$$

$$\frac{\partial u}{\partial t}+L(u)-\gamma v-\frac{uv\tan\phi}{R} =-\frac{g}{R\cos\phi}\frac{\partial \xi}{\partial \lambda}+\frac{\partial}{\partial z}\left(A_v\frac{\partial u}{\partial z}\right)+A_h\nabla^2 u, \tag{2}$$

$$\frac{\partial v}{\partial t}+L(v)+\gamma u+\frac{u^2\tan\phi}{R} =-\frac{g}{R}\frac{\partial \xi}{\partial \phi}+\frac{\partial}{\partial z}\left(A_v\frac{\partial v}{\partial z}\right)+A_h\nabla^2 v, \tag{3}$$

where t is the time, (u,v) are the velocity components in the zonal (λ) and meridional (ϕ) directions and ξ is the displacement at the surface, h is the mean water depth, γ is the Coriolis parameter, R is the radius of the earth, g is the gravity, A_v is the vertical eddy viscosity coefficient and A_h is the horizontal eddy viscosity coefficient. The advection operators $L(u)$ and $L(v)$ are

$$L(u)=\frac{u}{R\cos\phi}\frac{\partial u}{\partial \lambda}+\frac{v}{R}\frac{\partial u}{\partial \phi}+w\frac{\partial u}{\partial z},$$
$$L(v)=\frac{u}{R\cos\phi}\frac{\partial v}{\partial \lambda}+\frac{v}{R}\frac{\partial v}{\partial \phi}+w\frac{\partial v}{\partial z}, \tag{4}$$

where z is the vertical coordinate and w is the vertical component of velocity, both are positive downward from the sea surface. The horizontal diffusion terms $\nabla^2 u$ and $\nabla^2 v$ are given by

$$\nabla^2 u=\frac{1}{(R\cos\phi)^2}\left[\frac{\partial^2 u}{\partial \lambda^2}+\frac{\partial}{\partial \phi}\left(\cos\phi\frac{\partial u}{\partial \phi}\right)\right],$$
$$\nabla^2 v=\frac{1}{(R\cos\phi)^2}\left[\frac{\partial^2 v}{\partial \lambda^2}+\frac{\partial}{\partial \phi}\left(\cos\phi\frac{\partial v}{\partial \phi}\right)\right]. \tag{5}$$

Following Lee et al. (2000), we determine the current profiles by the Galerkin function method and assume two different structures according to the water depth, that is, a one-layer structure in shallow sea regions where the depth is less than a certain depth, h_1, and a two-layer structure (the upper layer thickness is h_1 and the lower layer thickness, $h-h_1$) in deep sea regions where the depth is greater than h_1 and an empirical function is introduced to expand the current profiles in the lower layer. We seek solutions in the form if $z \leqslant h_1$:

$$u(\lambda,\phi,z,t)=u_1(\lambda,\phi,z,t)=\sum_{j=1}^{m}\hat{u}_{1j}(\lambda,\phi,t)f_j(z), \quad \text{if } z\le h_1, \tag{6}$$
$$v(\lambda,\phi,z,t)=v_1(\lambda,\phi,z,t)=\sum_{j=1}^{m}\hat{v}_{1j}(\lambda,\phi,t)f_j(z),$$

$$u(\lambda, \phi, z, t) = u_2(\lambda, \phi, z, t) = u_1(\lambda, \phi, h_1, t)G(z)$$
$$= \sum_{j=1}^{m} \hat{u}_{1j}(\lambda, \phi, t) f_j(h_1) G(z),$$
$$v(\lambda, \phi, z, t) = v_2(\lambda, \phi, z, t) = v_1(\lambda, \phi, h_1, t)G(z)$$
$$= \sum_{j=1}^{m} \hat{v}_{1j}(\lambda, \phi, t) f_j(h_1) G(z), \qquad \text{if } z > h_1 \quad (7)$$

where $f_j(z)$ is the jth basis function and $\hat{u}_{1j}(\lambda, \phi, t)$ and $\hat{v}_{1j}(\lambda, \phi, t)$ are the corresponding coefficients, respectively, m is the number of basis functions. Following Lee et al. (2000), it is assumed that the empirical function $G(z)$ in Eq. (7) which accommodates the rapid decrease in the magnitude of the oceanic current in the lower layer takes the form

$$G(z) = \exp\left[-\alpha\left(\frac{z - h_1}{h_e}\right)^2\right], \quad (8)$$

where α is a constant and h_e is the e-folding depth of velocity in the lower layer. The choice of basis functions is arbitrary but in this study, a set of linear interpolation functions is chosen with smaller supports than the high-order B-splines used by Davies (1977a, b, 1978), forming narrower-banded matrices.

2.2. Boundary conditions

At the land boundary, the normal component of current is set to zero throughout the computation and a slip condition is imposed. Along the open sea boundaries a radiation condition based on Flather (1976) is used. For the open boundary directed to the east,

$$\bar{u} - \bar{u}_m - \bar{u}_T = \frac{\sqrt{gh}}{h}(\xi - \xi_m - \xi_T), \quad (9)$$

where $\bar{u}$ is the depth-averaged velocity at the open boundary, $\bar{u}_m$ and ξ_m are time-invariant velocity and elevation associated with oceanic flows, respectively, $\bar{u}_T$ and ξ_T are tidal velocity and elevation, respectively. $\bar{u}_m$, ξ_m, $\bar{u}_T$ and ξ_T are quantities prescribed a priori. In addition to Eq. (9), the internal velocity component, $(u - \bar{u})$, at the open boundary is extrapolated from the nearest interior grid point as a part of the radiational boundary calculation.

In order to solve the system of equations (1)–(3) for the dependent variables ξ, u and v, boundary conditions have to be specified at the sea surface and the sea bed. External stress is assumed to be zero at the sea surface and, at the sea floor, the following slip boundary condition is used:

$$\left[A_v \frac{\partial u}{\partial z}\right]_h = \frac{\tau_{b\lambda}}{\rho_o}, \quad \left[A_v \frac{\partial v}{\partial z}\right]_h = \frac{\tau_{b\phi}}{\rho_o}, \quad (10)$$

where $\tau_{b\lambda}$ and $\tau_{b\phi}$ are components of the bottom frictional stress in the λ and ϕ directions, respectively, and ρ_o is the density of seawater. The usual quadratic law is used for bottom friction:

$$\tau_{b\lambda} = \rho_o C_d u_b \sqrt{u_b^2 + v_b^2}, \quad \tau_{b\phi} = \rho_o C_d v_b \sqrt{u_b^2 + v_b^2}, \quad (11)$$

where C_d is the bottom drag coefficient, and u_b and v_b are the zonal (λ) and meridional (ϕ) components of velocity at the bottom, respectively.

2.3. The form of eddy viscosity

The horizontal eddy viscosity, A_h, is set to $100\,\mathrm{m^2/s}$. We use the flow-related vertical eddy viscosity, A_v, suggested by Davies and Aldridge (1993). That is,

$$A_v = 0.0025 D(\bar{u}^2 + \bar{v}^2)^{1/2}, \quad (12)$$

where

$$D = \frac{0.4}{\varpi_1} u_* \quad (D = h \text{ for } D \geqslant h), \quad (13)$$

with ϖ_1 being the characteristic frequency (1.0×10^{-4}), $\bar{u}$, $\bar{v}$ the depth-averaged horizontal components of oceanic currents, u_* the frictional velocity $(= \sqrt{\tau_b/\rho})$.

2.4. Model domain and computation

Fig. 1a shows the model area covering the entire shelf seas of the YS and the ECS and the Okinawa trough where the water depth is greater than 2000 m. The southern boundary lies near northern Taiwan at approximately 25°N, the eastern open boundary is near Korea/Tsushima Straits at about

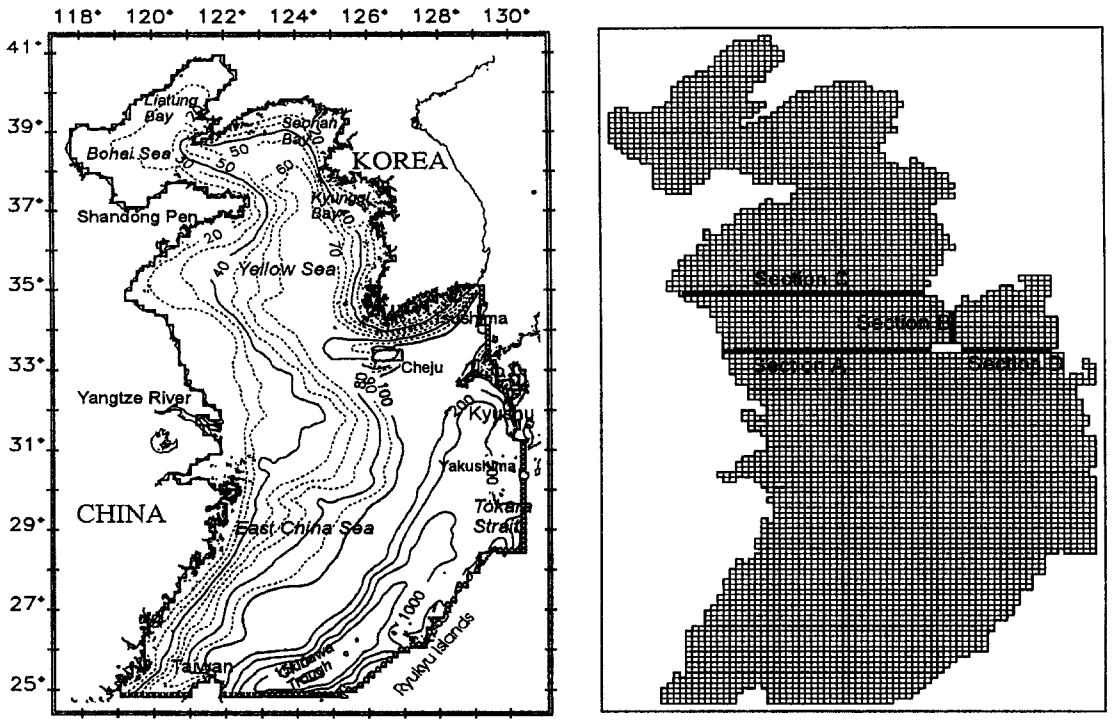

Fig. 1. Geographical locations and bottom topography of the Yellow Sea and the East China Sea (left); model grid (right) showing the cross sections where the volume transport is to be presented.

131°E and the southeastern open boundary is along the chain of Ryuku Islands. Model domain and depth field coincide with those used in Lee et al. (2000). Circles and cross symbols in the figure represent the inflow and the outflow open boundaries, respectively. The amplitudes and phases of M_2 tidal constituent along the open boundary are obtained from the result of Lee and Jung (1996). Fig. 1b shows the finite-difference grid showing three cross sections where the volume fluxes are to be estimated. The latitudinal and longitudinal grid intervals are 1/6° and 1/8°, respectively.

In this study, we take linear interpolation functions as a basis set and solve Eqs. (1)–(3) with a subdomain Galerkin method described in Lee et al. (2000). The thickness of the oceanic current, h_1, is again set to be 300 m based on the previous measurements (Kaneko et al., 1990; Ichikawa and Beardsley, 1993). The model has 11 nodes in the vertical and $\alpha = 4$ is used. Details on the numerical solution can be found in Lee et al. (2000). The time integration interval is set to be 124 s to satisfy the CFL condition. The model run is started from the state of no motion, that is, $\xi = 0$, and $u_1 = v_1 = 0$, subsequently $u_2 = v_2 = 0$. Following Lee et al. (2000), the oceanic influx through the Taiwan Strait and the Kuroshio volume transport through the shelf break east of Taiwan are given as 2.1 and 23 Sv, respectively. Futhermore, $\bar{u}_m$ and ξ_m in the radiational calculation are prescribed by the results of Exp. 1 of Lee et al. (2000) which is the calculation with a quadratic bottom friction formula, ignoring the background tidal effects. The tidal elevation ξ_T along the open boundary is harmonically generated using the M_2 harmonics used by Lee and Jung (1999, 1996).

The radiational calculation is implemented in three steps. The first step is to assume that $\bar{u}_m = \xi_m = 0$ and determine the depth-mean tidal velocity by solving the continuity equation in a

reverse way. The second step is to define $\bar{u}_m$ and ξ_m at the open boundary along with $\bar{u}_T$ and ξ_T and apply the radiation condition which is given, on an Arakawa C-grid with grid resolution of $\Delta\lambda$ and $\Delta\phi$, by

$$\bar{u}(\lambda_o + \Delta\lambda/2, \phi_o, t) = \bar{u}_m(\lambda_o - \Delta\lambda/2, \phi_o) + \bar{u}_T(\lambda_o - \Delta\lambda/2, \phi_o, t) + \frac{\sqrt{gh}}{h}(\xi(\lambda_o, \phi_o, t) - \xi_m(\lambda_o, \phi_o) - \xi_T(\lambda_o, \phi_o, t)), \quad (14)$$

where $\bar{u}(\lambda_o + \Delta\lambda/2, \phi_o, t)$ and $\xi(\lambda_o, \phi_o, t)$ are the depth-averaged velocity and the sea surface elevation computed at the open boundary cell, $\bar{u}_m(\lambda_o - \Delta\lambda/2, \phi_o)$ and $\xi_m(\lambda_o, \phi_o)$ are the depth-averaged velocity and the sea surface elevation, respectively, prescribed at the nearest interior grid. Details as to how to prescribe $\bar{u}_m$ and ξ_m can be found in Lee et al. (2000). The final step is to assign to $\bar{u}(\lambda_o + \Delta\lambda/2, \phi_o, t)$ the depth-varying components computed at the nodes ($z = z_{ej}, j = 1, \ldots, m$) of the nearest interior grid. This extrapolation procedure can be formally expressed by

$$u(\lambda_o + \Delta\lambda/2, \phi_o, z_{ej}, t) = \hat{u}_{1j}(\lambda_o + \Delta\lambda/2, \phi_o, t) f(z_{ej}) = \bar{u}(\lambda_o + \Delta\lambda/2, \phi_o, t) + [\hat{u}_{1j}(\lambda_o - \Delta\lambda/2, \phi_o, t) f(z_{ej}) - \bar{u}(\lambda_o - \Delta\lambda/2, \phi_o, t)] \quad (15)$$

with $j = 1, \ldots, m$. In Eq. (15), note that $f(z_{ej}) = 1$ for all j. The radiation routine is passed after solving the continuity equation, giving the velocity normal to the open boundary.

3. Results

A total of 9 numerical calculations have been performed in this study (see Table 1). Note that Calcn. 1–6 do not consider oceanic inflows and outflows. The optimum value of the bottom drag coefficient which gives rise to results most accordant with the observed tidal and tidal current data is determined through Calcn. 1–4. The effects of specifying a characteristic water depth, h_1, are examined through Calcn. 5 and 6 which take different values of a maximum water depth without considering $G(z)$. In Calcn. 7, we calculate the oceanic current in the presence of M_2 tide. Finally, the effects of spring–neap modulation of tide and seasonal variation in oceanic inflows/outflows on the circulation in the southern YS are examined in Calcn. 8 and 9, respectively.

Table 1
Description of numerical calculations

	C_d	External forcing	h_1 (m)	Comments
Calcn. 1	0.0025	M_2 tide	300	With $G(z)$
Calcn. 2	0.0035	M_2 tide	300	With $G(z)$
Calcn. 3	0.0050	M_2 tide	300	With $G(z)$
Calcn. 4	0.0075	M_2 tide	300	With $G(z)$
Calcn. 5	0.0035	M_2 tide	—	$h_{max} = 300$ m without $G(z)$
Calcn. 6	0.0035	M_2 tide	—	Real depth without $G(z)$
Calcn. 7	0.0035	M_2 tide + oceanic currents	300	With $G(z)$
Calcn. 8	0.0035	Spring–neap modulation of M_2 tide + oceanic currents	300	With $G(z)$
Calcn. 9	0.0035	M_2 tide + seasonal variation of oceanic currents	300	With $G(z)$

3.1. Tidal computation and comparison of the model results with observed data

A total of 71 M_2 tidal elevation harmonics which have been compositely constructed on the basis of the previous studies (Choi, 1980; Kang et al., 1998) and a total of 14 M_2 tidal currents harmonic data which were measured over 10 days or more by Harkema and Hsueh (1987), Larsen et al. (1985) and Huh et al. (1985), respectively, are used to compare with model results. The locations of current measurement stations are shown in Fig. 2 and information on the measurement details of the tidal current data are given in Table 2. The water depths of stations M4, MS and SB in Table 2

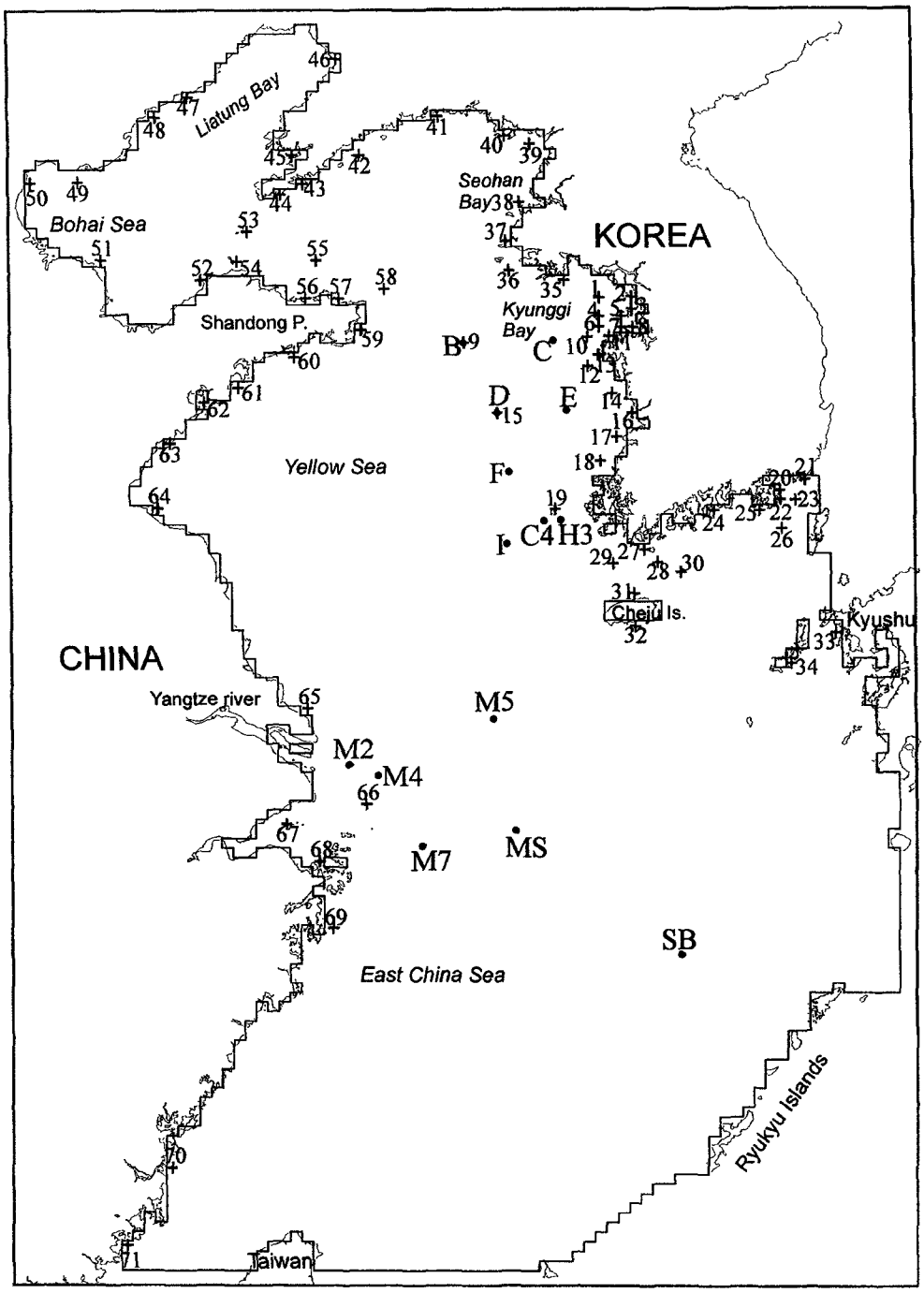

Fig. 2. Location of M_2 tide and tidal current measurement stations.

were obtained from Sternberg et al. (1983) and Beardsley et al. (1983) and estimations of water depth were made for stations M2, M5 and M7 on a bathymetric chart in terms of their longitudes and latitudes. A total of 34 tidal stations data (stations 1–34 in Fig. 2) are due to Kang et al. (1998) and the rest (stations 35–71 in Fig. 2) are due to Choi (1980). Harmonic constants of M_2 tide

Table 2
Details of tidal current data around the Yellow Sea and the East China Sea

Station	Lat. (deg)	Lon. (deg)	First record date (observation period)	Water depth (m)	Source of data
B	36.95	124.08	1986. 1. 13 (60 days)	75	Harkema and Hsueh (1987)
C	36.95	125.41	1986. 1. 12 (54 days)	53	Harkema and Hsueh (1987)
D	36.00	124.58	1986. 1. 12 (60 days)	87	Harkema and Hsueh (1987)
E	36.03	125.60	1986. 1. 13 (60 days)	64	Harkema and Hsueh (1987)
F	35.23	124.74	1986. 1. 13 (60 days)	96	Harkema and Hsueh (1987)
I	34.30	124.69	1986. 1. 12 (30 days)	94	Harkema and Hsueh (1987)
H3	34.58	125.50	1984. 3. 5 (32 days)	63	Huh et al. (1985)
C4	34.58	125.28	1982. 9. 16 (11 days)	65	Huh et al. (1985)
M2	31.39	122.37	1981. 8. 2 (12 days)	18[a]	Larsen et al. (1985)
M4	31.25	122.77	1981. 8. 5 (10 days)	47	Larsen et al. (1985)
M5	32.00	124.50	1981. 8. 3 (10 days)	39	Larsen et al. (1985)
M7	30.33	123.44	1981. 8. 4 (10 days)	65[a]	Larsen et al. (1985)
MS	30.52	124.80	1980. 6. 3 (21 days)	49	Larsen et al. (1985)
SB	28.91	127.25	1980. 6. 2 (32 days)	188	Larsen et al. (1985)

[a] The depths were read from bathymetric charts.

and tidal current have been extracted by analyzing model results with a Fourie analysis method, which were stored at a half lunar hour interval during the final 12 lunar hours after 25 iteration days.

To check the accuracy of the model, we calculate a parameter H_s, defined in Davies et al. (1997), as well as RMS errors in amplitude and phase. That is,

$$H_s = \frac{1}{n}\sum_{i=1}^{n} \{(HC_i)^2 + (HS_i)^2\}^{1/2} \tag{16}$$

with n being the number of tidal observations and

$$HC_i = A_{oi}\cos(g_{oi}) - A_{ci}\cos(g_{ci}),$$
$$HS_i = A_{oi}\sin(g_{oi}) - A_{ci}\sin(g_{ci}), \tag{17}$$

where A_{oi} and g_{oi} are the observed amplitude and phase lag, and A_{ci} and g_{ci} computed at the ith station.

Fig. 3 displays scatter plots of tidal amplitude and phase lag referred to 135°E. It is noted that the increase in the bottom frictional coefficient (0.0025–0.0075) gives rise to a decrease in the M_2 tidal amplitudes but produces very little change in the phases. From the result of Calcn. 4, it is apparent that the amplitudes are considerably underestimated throughout the stations. Results from Calcn. 2 and 3 are in good agreement with observations even though the amplitudes are slightly underestimated along the Chinese coast (stations 41–71) in the case of Calcn. 3 and are overestimated in Kyunggi bay (stations 1–8) in the case of Calcn. 2. Model runs with additional tidal constituents might improve the accuracy in the west coast of Korea, yielding more bottom friction in Kyunggi Bay and hence resulting in smaller amplitudes of M_2 tide. There are many possible sources for the relatively large errors occurring on the Chinese coast. There may be a problem of the time zone, but it is more likely that the errors in water depth can be a prime reason. The abnormally large error at Site 47 may be attributed to the fact that the site is located near the degenerated amphidromic point.

Table 3 shows RMS errors and H_s errors (note that errors are defined by observed minus computed ones). A total of 70 points, excluding the data at station 47 showing an exceptionally large deviation, have been used for comparison. It is evident that use of different bottom frictional coefficients from Calcn. 1 to 4 overpredicts (negative values) or underpredicts (positive values) the tidal amplitudes by noticeable amounts but phase lags are much less sensitive to the change in the bottom frictional coefficient. The best results have been obtained from Calcn. 2 in which RMS

errors of amplitude, phase lag reduce to 16.4 cm, 19.5° and H_s error is 39.5. In the results of Lee and Jung (1999), RMS errors were minimum when the bottom frictional coefficient 0.0038 was used with the same flow-related vertical eddy viscosity.

As a way of representing the stratified structure of current profiles in the Kuroshio main stream in deep sea regions, we have introduced an empirical function which decreases exponentially through the depth. It is obvious that this treatment results in a distortion of the propagation of a barotropic tidal wave and the associated volume flux. We consider two cases: one is to fix the maximum depth as 300 m (Calcn. 5) and another is to use a

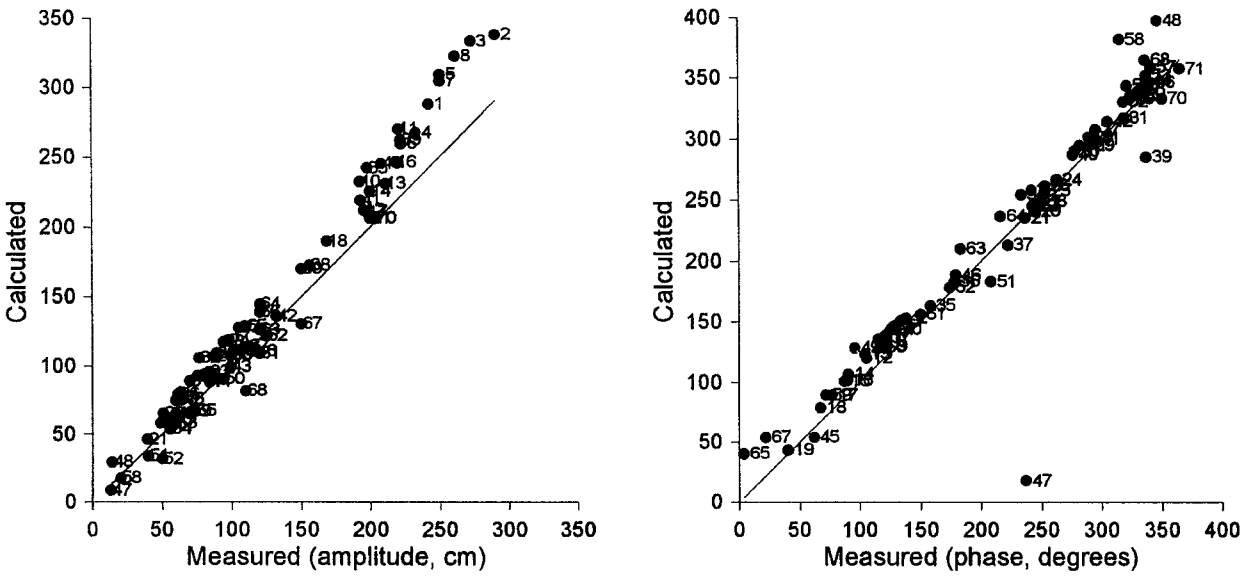

(a)

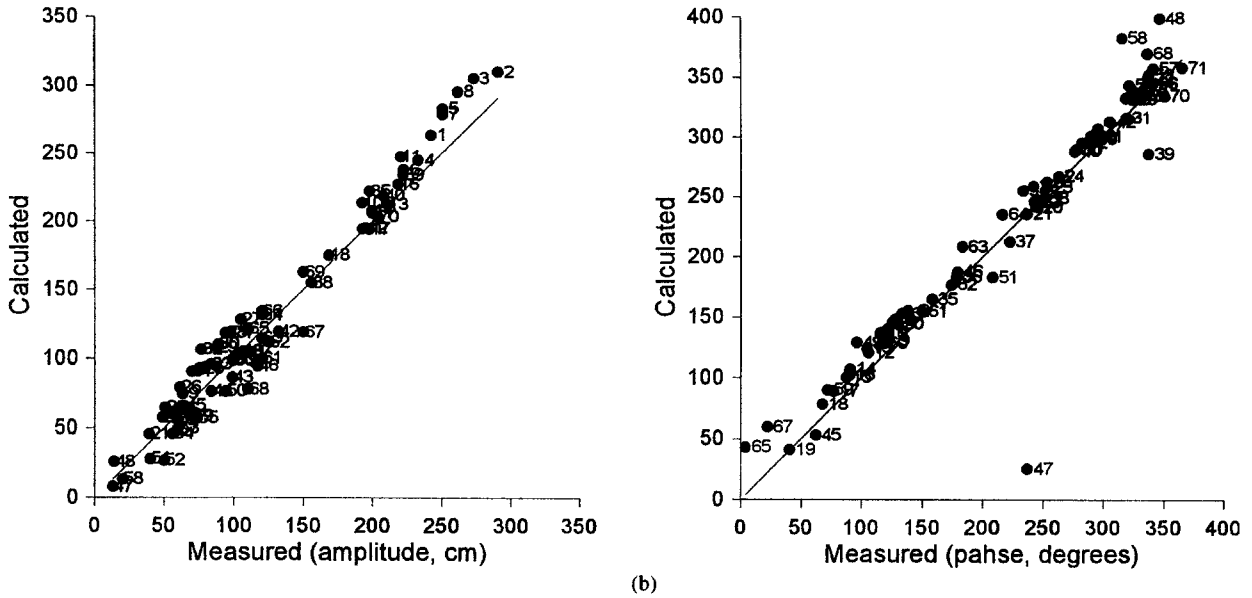

(b)

Fig. 3. Comparison between observed data and calculated values from (a) Calcn. 1, (b) Calcn. 2, (c) Calcn. 3 and (d) Calcn. 4.

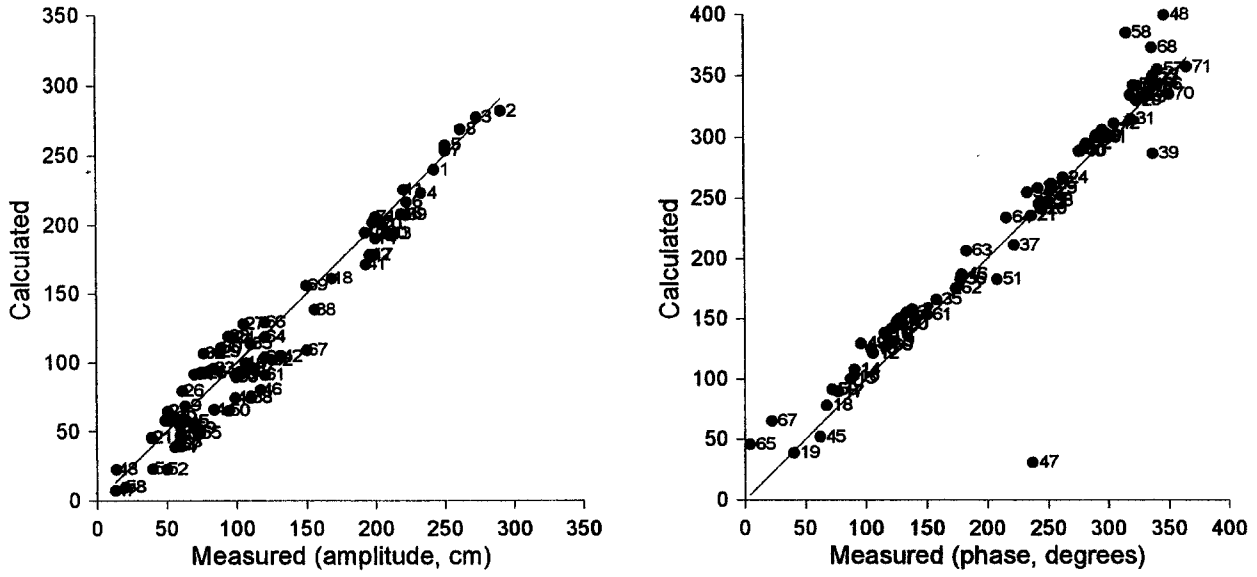

(c)

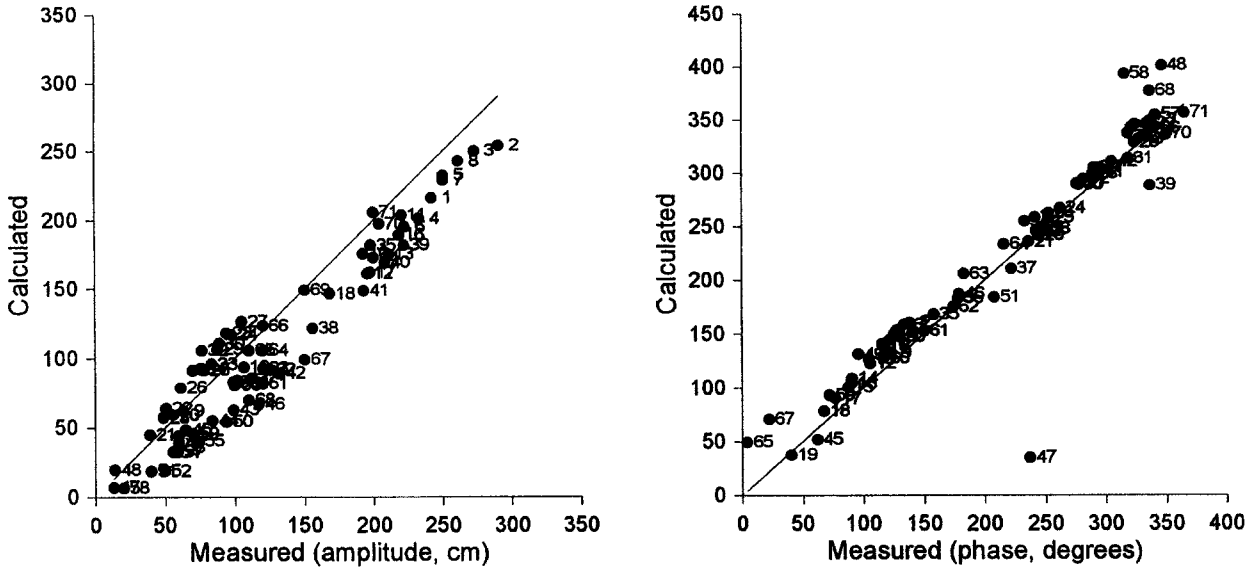

(d)

Fig. 3. (*Continued.*)

real topography (Calcn. 6). In both cases $G(z)$ is not used and the bottom frictional coefficient is fixed as 0.0035. As a consequence, RMS errors decrease to 13.9 cm, 15.0° in Calcn. 6 but increase to 18.9 cm, 25.0° in Calcn. 5. Differences in RMS errors between Calcn. 5 and 6 are 5.0 cm in amplitude and 10.0° in phase. Compared with the data on the Korean side, Calcn. 2 gives amplitude and phase errors of 18.6 cm and 14.0°, respectively, while Calcn. 6 gives 13.5 cm and 5.7°, respectively. It is noted that the phase errors are markedly reduced. In Kang et al. (1998) calculations using a 2D fine-grid model (with resolution of 1/12° latitude, 1/16° longitude) forced by five

Table 3
Distribution of the number of points where difference (observed−computed) in the M_2 tidal elevation amplitude (Δa) and phase (Δg) lies within ± 5 cm and $\pm 5°$

Calcn.		<−20	−20	−15	−10	−5	5	10	15	20	>20	RMS error	Error (H_s)
1	Δa	24	11	6	8	7	7	3	1	2	1	24.8 cm	41.9
	Δg	11	14	16	11	8	4	3	0	1	2	19.0°	
2	Δa	15	4	12	6	7	7	4	8	3	4	16.4 cm	39.5
	Δg	13	12	15	12	8	4	3	0	1	2	19.0°	
3	Δa	7	2	3	10	6	3	10	6	12	11	17.2 cm	41.5
	Δg	17	11	13	11	7	5	2	2	0	2	20.4°	
4	Δa	5	4	3	4	2	3	1	3	10	35	25.8 cm	46.6
	Δg	22	7	14	10	6	4	2	2	0	2	21.9°	
5	Δa	18	9	8	4	11	3	5	5	3	4	18.9 cm	53.8
	Δg	34	12	9	4	3	4	1	1	1	1	25.0°	
6	Δa	3	10	8	8	7	6	10	8	5	5	13.9 cm	24.9
	Δg	6	1	1	16	19	13	7	2	2	3	15.0°	

constituents M_2, S_2, K_1, O_1 and N_2, the RMS amplitude and phase errors of M_2 tide were 9.7 cm and 4.5°, respectively. Use of a multi-constituent fine-grid model clearly improved the accuracy of the tidal amplitudes but not the phase. It is noted in his verification that the accuracy of the model was checked through the comparison with the data along the Korean and Japanese coasts.

We briefly comment on the effect of oceanic currents on the M_2 tidal harmonics computed with Calcn. 7. The RMS amplitude and phase errors in the presence of oceanic currents are 16.2 cm and 19.9°, respectively. The distribution of tidal elevation harmonics of Calcn. 7 is not presented, but close examination reveals that reduction by about 0.5–1 cm occurs throughout the YS and in the southeastern ECS. The M_2 tidal elevation harmonics increase by similar amount on the southwestern corner of the ECS.

Fig. 4 displays the tidal chart computed with Calcn. 2. Solid and dotted lines denote co-tidal lines and the co-amplitude lines, respectively. The general pattern of the tidal chart shows generally a good agreement with existing tidal charts, for example, Nishida (1980) and Fang (1986), even though the amphidrom in Liatung Bay appears in a slightly degenerated form. Similar results were obtained in previous numerical calculations (Guo and Yanagi, 1998; Kang et al., 1998; Lee and Jung, 1999). It is noted that the model has a tendency to overestimate tidal amplitudes in regions such as

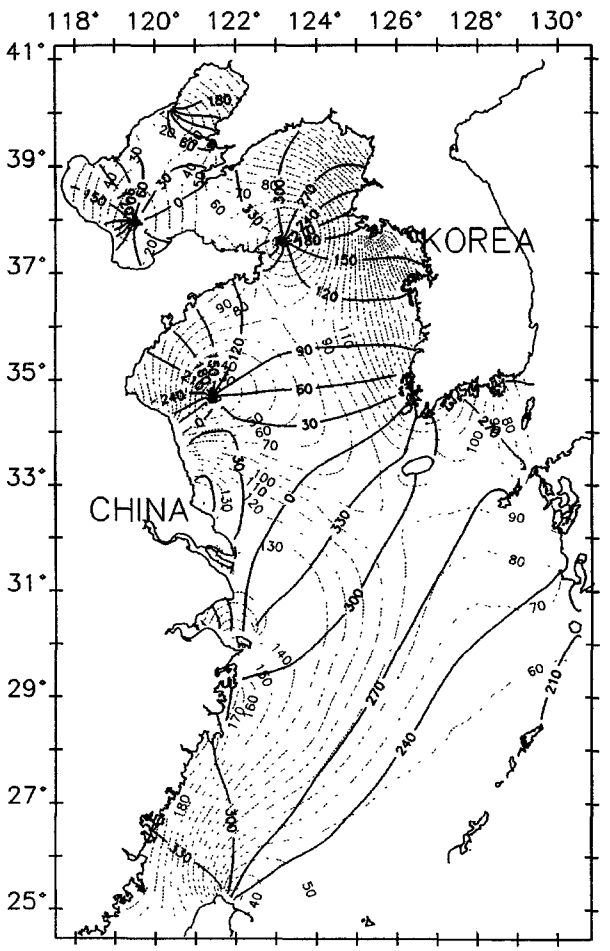

Fig. 4. M_2 tidal chart computed from Calcn. 2 with co-range lines (dashed line) and co-phase lines (solid line). Phase lags in degree refer to 135°E.

along the south coast of Korea and around Cheju Island. The tendency also appeared in previous calculations (Lee and Jung, 1996, 1999; Kang et al., 1998; Guo and Yanagi, 1998). Blain (1997) simulated with better accuracy the M_2 tide in the vicinity of Cheju Island but with tidal inputs 50% smaller than the observed tides (there are considerable amounts of tidal data near the eastern open boundary on both sides of Korea and Japan, and at the center of the Strait).

Without presenting co-tidal and co-phase lines of Calcn. 5 and 6, we describe differences in some detail. Limiting the depth of Okinawa trough to 300 m greatly alters the entire response of the YS and the ECS although the amphidromic points are formed virtually at the same positions. Calcn. 5 overpredicts the tidal amplitudes compared to Calcn. 6, as seen in the results of RMS errors. The phase lines of Calcn. 6 in the ECS advance by about 25° than Calcn. 5, while in the YS and the ECS by about 15°. Of course, this is because the depth determines the phase speed, that is, $\sqrt{gh}$. Results from Calcn. 2 are approximately in between (retarded about 12°, compared with Calcn. 6 in Okinawa trough). We can see that the approach using the empirical function accommodates to some extent the bottom topography. The accuracy of the present model for the M_2 elevation is better than that of Guo and Yanagi (1998) where the error H_s was 61.2 or more and comparable to that of Lee and Jung (1999) where RMS errors of amplitude and phase were 14.04 cm and 15.46°, respectively. Consequently, we have decided to use the parameters of Calcn. 2 for the simulation of M_2 tide with oceanic currents, that is, Calcn. 7.

Table 4 summarizes observed and computed amplitudes and phases of u and v components at the 14 stations given in Table 2. It is noted that the model reproduces u and v current with varying accuracy. The observed tidal current shows considerably different current profiles according to the measured time, that is, summer (stations B–C4) or winter season (stations H3–SB). We can see that there are nearly 200° changes in the observed phase lags of v component of tidal current and 40 cm/s changes in amplitude at station M2 which is located close to the mouth of the Yangtze River and a similar tendency is also shown in C4. Surprisingly, however, the result measured in March 1984 at station H3, which is located close to station C4, shows variations in amplitude and phase less than 10 cm/s and 10°, respectively. River discharge and baroclinic effects, which have not been included in this model, might influence the vertical structure of the tidal current, producing considerable discrepancy between the observed and computed harmonics (more precisely amplitudes and phase lags at C4 and M2, phase lags at M5). See Lee and Jung (1999) for more detailed discussions. RMS errors of Calcn. 2 are 9.1 cm/s, 28.7° and 12.1 cm/s, 49.2° in u and v components of tidal currents. RMS errors calculated with 7 stations (stations B–H3) decrease to 8.0 cm/s, 29.6° and 11.6 cm/s, 12.1°, while RMS errors with the remaining 7 stations (stations C4–SB) increase to 10.2 cm/s, 28.9° and 12.6 cm/s, 62.4° except phase lags in u component of tidal currents. A similar accuracy has been obtained in the previous calculation by Lee and Jung (1999), although the model results are not directly comparable with each other.

3.2. Mean current field in the YS and the ECS

In order to examine the mean current field, an averaging of model results is required. It appears that there is some controversy in the literature regarding the proper procedure for computing residual currents. Nihoul and Runfola (1981) claimed that, in many regions, the computational error is comparable to the tidal residual current itself and hence it is necessary to solve time-averaged equations of motion with proper boundary values. In practice, however, researchers mostly solved time-dependent equations of motion and then averaged model results in two ways. One is a simple average of horizontal velocities over tidal period, the other is the flux average taking into account the time variation of total depth. Bowman and Chiswell (1982) calculated the Eulerian tidal residual current through the simple average of their two dimensional model results over a tidal period. Wolf (1987) presented, in the Bristol Channel and Severn Estuary study, the surface and bottom residual currents by simple

Table 4
Comparison of observed and computed amplitudes (cm/s) and phases (deg) of M_2 tidal current from Calcn. 2 at a number of depths and locations[a]

St.	Depth (m)	z (m)	u-amplitude (cm/s)		u-phase (deg)		v-amplitude (cm/s)		v-phase (deg)	
			OBS	CAL	OBS	CAL	OBS	CAL	OBS	CAL
B	75	38	18.6	19.7	17	45	32.8	28.7	159	165
		74	11.8	17.0	25	41	22.4	24.3	148	154
C	53	52	29.5	45.2	14	42	25.9	33.0	98	96
D	87	41	15.1	17.3	22	41	26.1	33.7	75	71
		86	15.4	16.4	21	25	17.0	27.0	72	64
E	64	63	20.1	28.0	358	18	25.4	36.9	52	63
F	96	70	5.0	9.5	19	39	39.9	45.8	31	36
		95	8.3	8.9	340	24	26.0	40.9	2	33
I	94	48	13.3	23.3	123	147	43.7	53.1	10	20
H3	63	20	10.7	22.1	117	149	64.8	86.5	4	13
		45	7.4	17.9	103	155	57.6	72.0	358	8
C4	65	15	6.0	20.2	141	144	70.6	77.5	6	20
		40	7.7	14.5	230	153	33.6	64.0	339	13
M2	18	4	84.0	61.8	120	126	83.4	51.6	115	354
		13	36.5	50.3	80	124	46.1	40.4	325	352
M4	47	25	40.1	43.7	101	114	40.6	46.9	331	346
		38	34.8	37.0	92	113	35.6	38.8	320	343
		44	30.0	34.5	89	113	33.7	35.8	316	342
M5	39	5	55.0	63.2	145	91	58.7	62.4	56	352
		20	47.3	59.2	69	90	50.8	58.0	333	351
		35	39.1	46.7	105	89	40.1	45.4	7	349
M7	65	5	39.7	42.7	77	71	43.0	56.8	326	317
		50	24.0	34.0	54	69	34.6	44.9	300	311
		60	19.1	31.4	85	69	26.9	41.3	325	310
MS	49	23	42.2	48.0	45	52	40.7	43.0	307	301
		32	35.5	42.5	22	51	33.8	37.6	282	299
		45	31.8	36.9	33	49	30.0	32.1	293	297
SB	188	177	26.7	13.5	12	8	16.8	12.7	232	238

[a] Note: Phase lags are referred to 135°E. z means the mooring depth.

averaging over M_2 tidal cycle of three-dimensional model results in each layer. On the other hand, Backhaus (1979) calculated residual flows using the flux average in three-dimensional barotropic modeling of tidal- and wind-driven circulation of German Bight. Two definitions were tested and we have found that the flux average gives more realistic results in view of mass balance. In this study, residual flows are calculated as follows:

$$\bar{u}_j = \frac{\int_0^T \int_{-\xi}^h \hat{u}_{1j} f_j(z)\,dz\,dt}{\int_0^T \int_{-\xi}^h f_j(z)\,dz\,dt}, \quad \bar{v}_j = \frac{\int_0^T \int_{-\xi}^h \hat{v}_{1j} f_j(z)\,dz\,dt}{\int_0^T \int_{-\xi}^h f_j(z)\,dz\,dt}, \tag{18}$$

where $\bar{u}_j$ and $\bar{v}_j$ are the components of residual flows at the jth node, T is the M_2 tidal period.

Fig. 5 displays the mean flow fields at the sea surface obtained from Calcn. 7. We can readily see that the overall features coincide with Exp. 4 of Lee et al. (2000). The Kuroshio main stream flows along the continental slope approximately northeastward and turns southeastward near the shelf break west of Kyushu toward the Tokara Strait on outer shelf regions of the ECS. The current field in shelf seas of the ECS and the branching near 29°30′N, 127°30′E are similarly found. Furthermore, a clockwise circulation is formed around the trough west of Kyushu and a

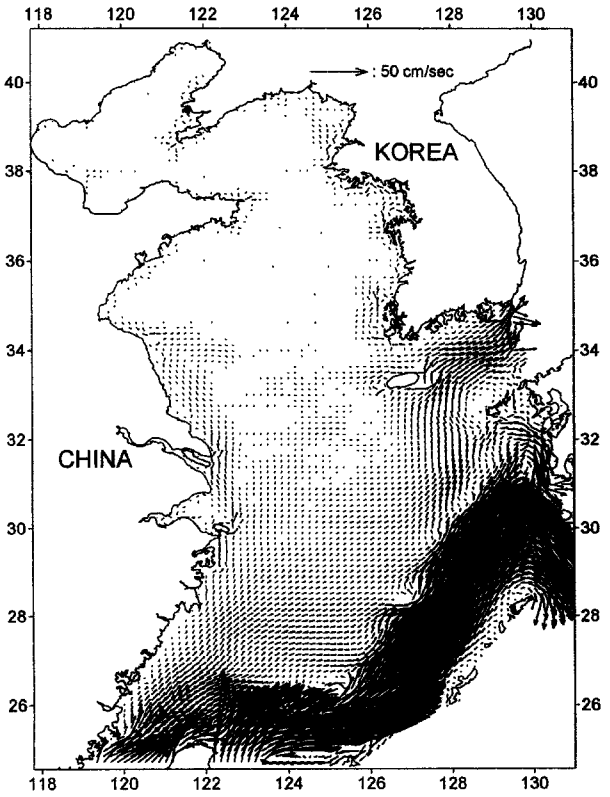

Fig. 5. Flow fields at the sea surface computed from Calcn. 7.

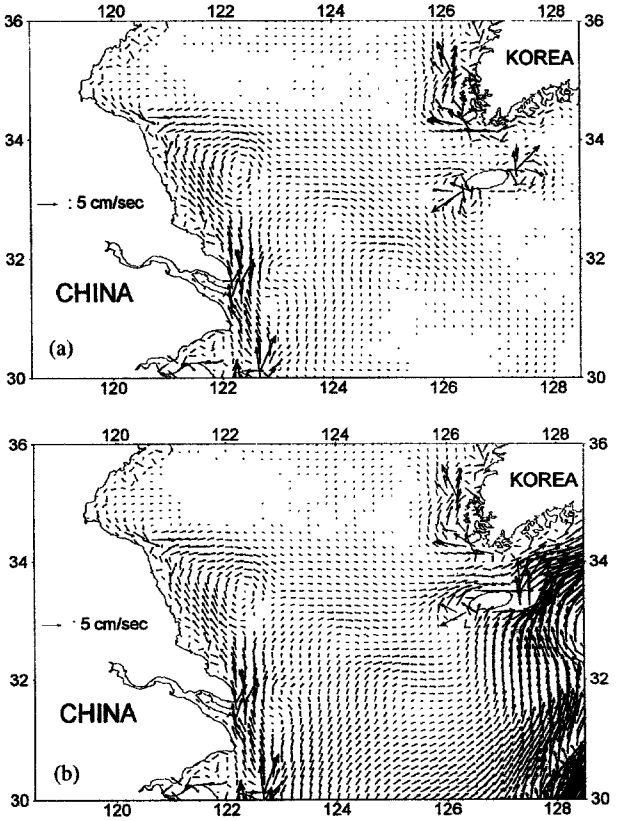

Fig. 6. Detailed sea surface flow fields west of Cheju Island computed from Calcn. 2 (upper) and Calcn. 7 (lower). Flow fields are time averaged over the M_2 tidal period using Eq. (18).

stronger flow in the western channel of Korea/Tsushima Straits than the eastern channel is clearly shown. Of course, both of them are qualitatively in very good agreement with recent observations by ARGOS buoy tracking (Lie and Cho, 1997). See Lee et al. (2000) for more detailed discussions on the flow fields.

We now examine in more detail the flow field near Cheju Island and the southern YS. Fig. 6 displays the time-averaged sea surface flows computed with M_2 tidal forcings only (Calcn. 2) and with M_2 tidal forcing plus oceanic flows (Calcn. 7). The upper diagram in Fig. 6 therefore represents sea surface M_2 residual currents, the lower diagram represents the sea surface oceanic current superimposed on the M_2 residual current. The corresponding flow fields at the sea bottom are given in Fig. 7. The model result confirms the conclusion of a previous study (Lee et al., 1999) in that the flow entering the interior YS cannot be found. The present results also explain why no drifters released off southwest Cheju Island entered the YS (Beardsley et al., 1992; Lie and Cho, 1997). However, the flow pattern in the YS is quite different and the presence of M_2 residual flows is mainly the reason.

The results of Calcn. 2 display that headland eddies appear at the right and left tips of Cheju Island and near the southwest corner of the Korean Peninsula. We can also see that relatively strong northward residual flows are formed along the southwest coast of Korea and, as a compensation, weak southward flows are developed in the central YS. Similarly, tidal residual currents are apparently formed along the Chinese coast and, by continuity of mass, this is compensated by the formation of relatively strong southeastward residual flows in downhill regions with water depths of 30–70 m. We note that in the shallow

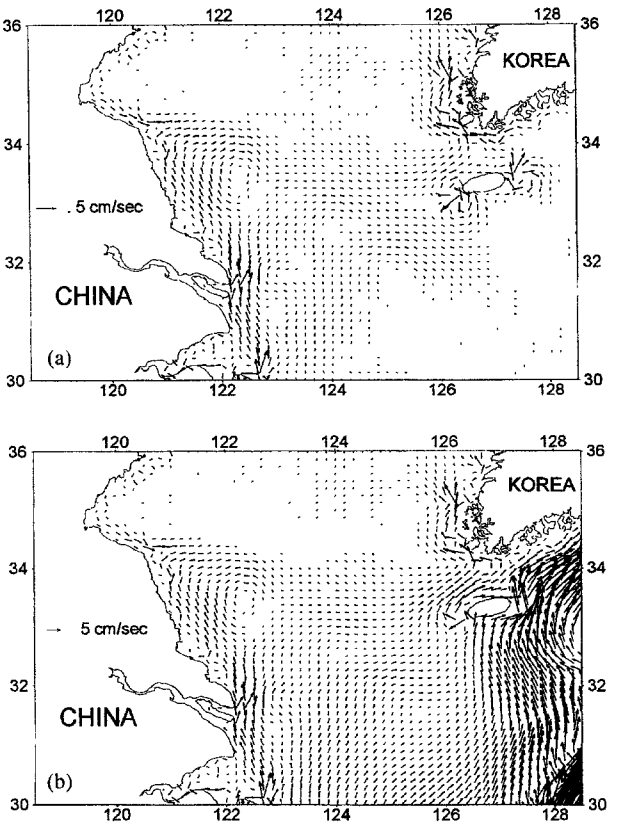

Fig. 7. Detailed sea bottom flow fields west of Cheju Island computed from Calcn. 2 (upper) and Calcn. 7 (lower). Flow fields are time averaged over the M_2 tidal period using Eq. (18).

sea regions off the Yangtze River tidal residual currents are approximately in the same direction with oceanic current and its magnitude reaches about 20–30% of the oceanic current.

Going further north, tidal residual flows dominate. It is interesting to note that three small gyres appear in a series on the 40 m depth contours. The gyre at the north is distinct, and two gyres downstream are relatively less distinct and smaller. The counterclockwise flows on the side of Korea and clockwise flows on the side of China merge with each other and, further downstream, with northward oceanic flows (more precisely, northward oceanic flow plus tidal residual flow). We note that tide-induced residual currents are small in the Cheju Strait. From Fig. 7, it is seen that the residual currents are not uniform through the water column. The bottom residuals are smaller than the surface residuals. The veering of the direction of the residual through depth is noted in the northwest of Cheju Island.

From the result of Calcn. 7, we see that northward oceanic flows deflect to the east, directing to Cheju Island instead of penetrating into the YS, which is consistent with the results of Exp. 4 of Lee et al. (2000). However, there is some difference. In Exp. 4 the northward oceanic flow starts to deflect to the east near 32°N, while Calcn. 7 generates relatively strong tidal residual currents extending further north up to 33°N, turning right very sharply and mostly crossing the isobaths with angles of about 90° or more, eventually merging with northward oceanic current. Due to the presence of tidal residual current, the volume transport across Section A decreases. The details of the volume transport will be discussed later.

3.3. Sea surface elevation in the YS and the ECS

Figs. 8 and 9 are the distributions of time-averaged sea surface elevation computed with Calcn. 2 and 7, respectively. The contour interval is 1.0 cm for negative values (dotted line) and 5 cm for positive values (solid line). It is noted from Fig. 8 that positive values appear on the left half of the YS, while negative values appear on the right half. It is interesting to note that semicircle-shaped contours are formed around the Seohan Bay, at the southwestern tip of Korea and at the Chinese coast between 32°N and 34°N. These are regions where large values of tidal residual flows are computed. From the results of Calcn. 7 shown in Fig. 9, the overall distribution of the sea surface elevation in the ECS is quite similar to Exp. 4 of Lee et al. (2000), but the sea surface elevations in the YS significantly differ from each other, particularly along the west coast of Korea and the Chinese coast. This is of course due to the residuals generated by tidal nonlinearities. At the western channel of the Korea/Tsushima Strait, the sea surface elevation is negative and its difference across the strait is more than 10 cm with a higher value on the right of flow direction, invoking the geostrophic adjustment.

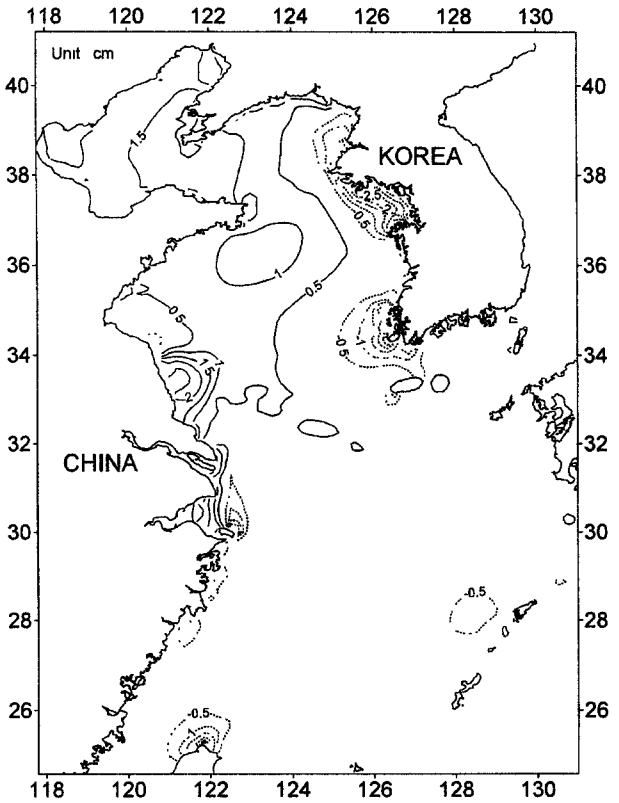

Fig. 8. Time-averaged sea surface elevation fields over the M_2 tidal period computed from Calcn. 2.

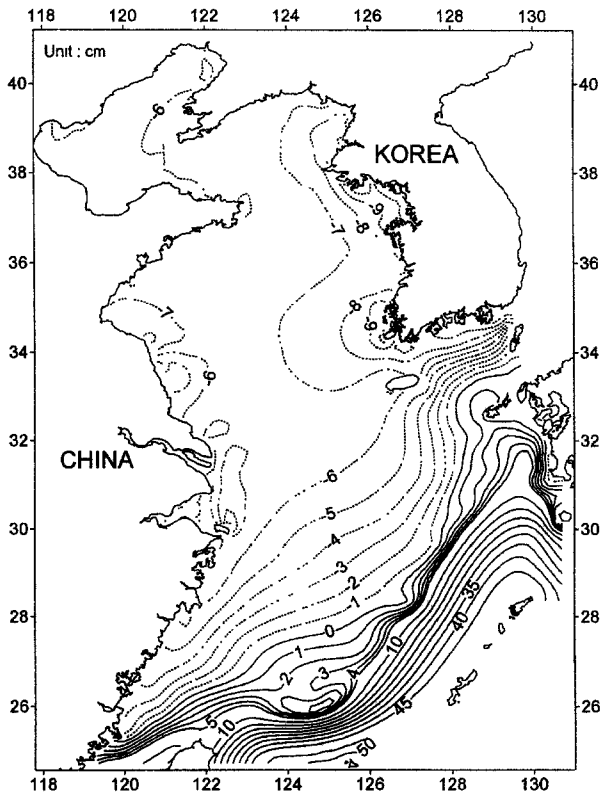

Fig. 9. Time-averaged sea surface elevation fields over the M_2 tidal period computed from Calcn. 7.

The sea surface elevation has positive values at the outer shelf of the ECS more than 45 cm near the open boundary along the chain of Ryukyu Islands. On the other hand, negative values ranging −6 to −10 cm occur in the inner YS, but there is in fact a very little spatial variation of the sea surface elevation when tidal nonlinearities are excluded. Exp. 4 of Lee et al. (2000) reproduced the same results. It is inferred that the strong bottom friction inhibits the formation of the sea surface elevation resembling the contours of isobath, consequently contributing to blocking of oceanic current intrusion into the YS.

We now compare the model result with the distribution of sea surface elevation deduced by Yanagi et al. (1997) from TOPEX altimetric data in the YS and the northern ECS. Yanagi et al. (1997) analyzed the data taken by TOPEX altimeter over 108 cycles from September 1992 to August 1995. For the TOPEX/POSEIDON tracks over the study region, see Fig. 1(b) in Yanagi et al. (1997). Initially, data are obtained at intervals of about 6.2 km along the satellite tracks (a total of 7 tracks in the YS and the ECS), but the data points differ every cycle. For that, the data observed in a cycle were linearly interpolated at the fixed points of 6.2 km intervals along the satellite track and averaging was further made over nine points to suppress small-scale phenomena. To estimate the absolute values of seasonal variation in sea surface dynamic topography in the study area, the mean surface dynamic topography was calculated based on the results from a diagnostic numerical model of the YS and the ECS given by Yanagi and Takahashi (1993). The model was forced by the observed distributions of temperature and salinity from the Marine Environmental Atlas (Japan Oceanographic Data Center, 1978) as well as wind stress calculated based on comprehensive ocean–atmosphere data set (COADS, Woodruff et al.,

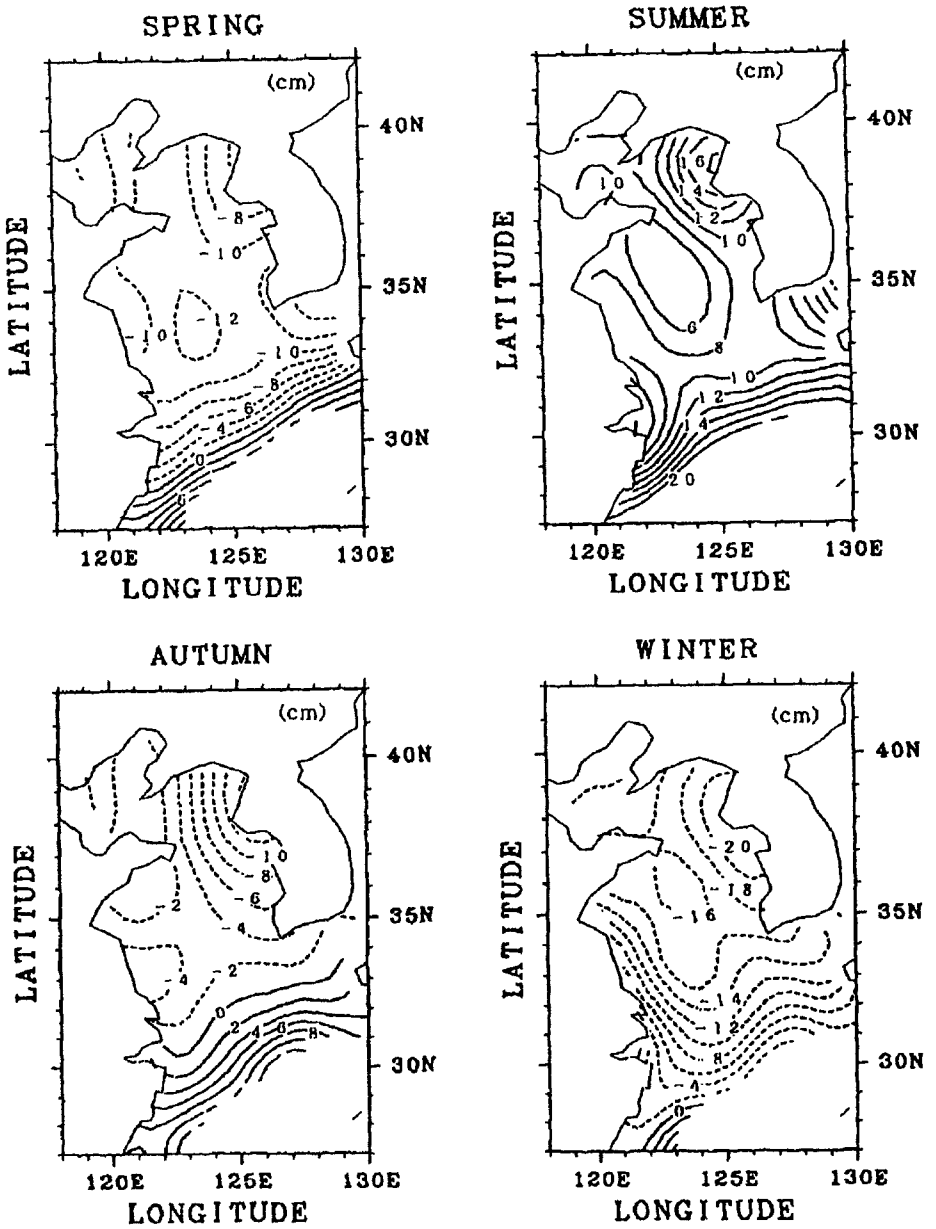

Fig. 10. Calculated sea surface elevation fields from the TOPEX-POSEIDON altimetric data (after Yanagi et al., 1997).

1987). However, the volume flux of Kuroshio was excluded. Despite the difference in the methodology of estimating the variation in the sea surface elevation, it is noted from Fig. 10 that the overall patterns are qualitatively similar to the model result. The sea surface is high approximately along the oceanic flow in the ECS with a maximum 20 cm in summer and low along the west coast of Korea with a minimum −20 cm in winter. In the central part of the YS the sea surface gradient is small and the minimum value reaches about −16 cm in winter. We note that the sea surface elevation increases to the coast of Seohan Bay in spring (March–May) and summer (June–August), while it decreases in autumn (September–November) and winter (December–February). The reason

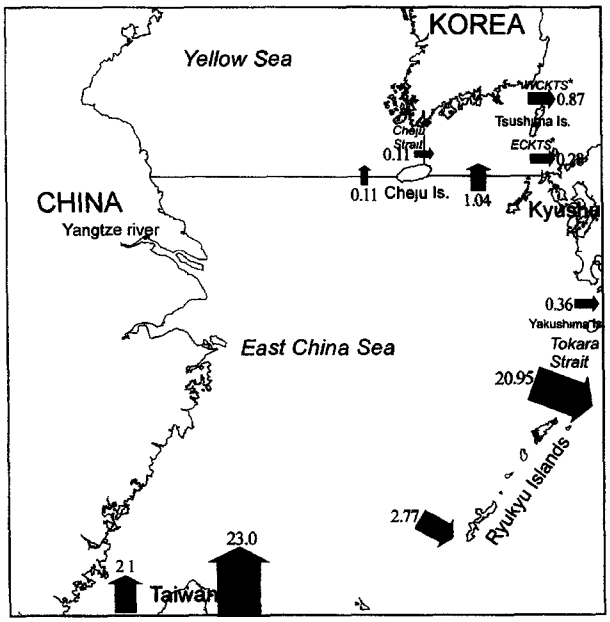

* WCKTS (Western Channel of Korea/Tsushima Strait)
ECKTS (Eastern Channel of Korea/Tsushima Strait)

Fig. 11. Calculated volume transports through the 3 cross sections and 5 openings. The unit for volume transport is Sv ($=10^6\,m^3/s$).

why the direction of the sea surface gradient changes with seasons needs to be explained in the future. According to Yanagi et al. (1997), the estimated error is about 3 cm in the sea and about 5–6 cm near the coast. It is worth commenting that in the calculation of Yanagi and Takahashi (1993) the bottom friction was represented in a quadratic form with use of 0.0026 as its coefficient. According to the present study, such a use can give rise to considerable errors in the sea surface elevation and current. Further research on this matter might be of great interest.

3.4. Volume fluxes across major cross sections

Fig. 11 shows the volume fluxes averaged over an M_2 tidal period at the 5 outflow openings (the eastern and western channels of the Korea/Tsushima Strait, north of Tokara Strait, Tokara Strait, Ryukyu Islands) and 3 cross sections (Sections A, B and D) shown in Fig. 1. The volume transport through the cross section west of Cheju Island (Section A in Fig. 1) is about 0.11 Sv and the same volume passes through the Cheju Strait. It is noted that the volume transport is reduced by 0.04 Sv, compared with that of Exp. 4 of Lee et al. (2000). The transport in an eastern section of Cheju Island (Section D in Fig. 1) is about nine times larger than that of the Cheju Strait. The calculated transport volume almost coincides with the value estimated by Candela et al. (1992) from ADCP measurements. The transport of Tsushima Warm Current (TWC) through the Korea/Tsushima Straits is about 1.15 Sv. The volume transport through the western channel is about three times larger than that through the eastern channel (0.87 Sv through the western channel and 0.28 Sv through the eastern channel). These results support the results of Yi (1966) and Kaneko et al. (1991).

The total amount of volume transport through the 5 outflow openings is estimated to be 25.23 Sv. The discrepancy between the inflow and outflow volume transports is therefore about 0.5% of the inflow volume through the southern open boundaries, about 11% of the calculated TWC volume transport. We surmise that corner boundaries located around Ryukyu Islands mostly cause errors in calculating the volume transport. The mass balance over the model domain indicates that the forced radiation condition has worked satisfactorily.

3.5. Sensitivities of oceanic circulation to A_h and α

We briefly describe, without showing the detailed figures, sensitivities of model results to some major parameters, especially the horizontal eddy viscosity A_h and the parameter α determining the shape of $G(z)$. Calculations with $A_h = 10$ and $1000\,m^2/s$ have reproduced basically the same circulation patterns with that computed with $100\,m^2/s$. Some local changes are, however, noticeable; reducing the horizontal eddy viscosity strengthens the return flow east of Taiwan, while increasing the horizontal eddy viscosity weakens it; the width of shelfward flows branching off the Kuroshio main stream increases and the gyre west of Kyushu forms over a larger area; decreasing the eddy viscosity results in the slightly steeper gradient of the sea surface elevation across the

Kuroshio main stream. The value of α, along with h_e, contributes to the determination of the trapping of Kuroshio at the upper ocean. Calculations with $\alpha=1$ and 10, fixing $A_h=100\,m^2/s$, show that changes in the overall pattern of circulation are very marginal; use of $\alpha=10$ slightly increases the width of the shelfward flows, compared with those computed with $\alpha=4$ and 10.

3.6. Effects of the spring–neap modulation of tide and the seasonal variation in oceanic inflows on the circulation in the YS

Up to now we have investigated the effects of M_2 tide on the oceanic circulation of the study area. The M_2 tide is indeed the most dominant constituent in the YS and ECS but it is noted that the magnitude of the S_2 tide amounts to about 30–40% of the M_2 tide. The spring–neap modulation in the bottom friction can therefore be considerably large, influencing somehow the formation of oceanic circulation as well as tide-induced residual currents. Furthermore, it is known that there is a substantial variation in the oceanic inflows through the Taiwan Strait and the shelf break east of Taiwan. According to Zhao and Fang (1991), the inflow at the Taiwan Strait reaches a maximum of about 3.1 Sv and a minimum of about 1.05 Sv. For the main stream of the Kuroshio, there appear a lot of discrepancy in estimates of the volume transport and its seasonal variation. Chen et al. (1992) estimated the volume transport of the Kuroshio to be 30 ± 2.0 Sv southwest of Kyushu. Ichikawa and Beardsley (1993) estimated the mean Kuroshio volume transport in the ECS to be 23.7 ± 2.0 Sv. Meanwhile, Yuan et al. (1994) estimated the volume transport to be about 14.5 Sv in April and 34.3 Sv in October northeast of Taiwan based on the hydrographic data measured during the period 1987–1989. In what follows, we therefore investigate the modulation effects on the circulation of the study area, again with emphasis on the circulation in the southern part of the YS. For that, the radiational condition at the open boundary is further modified. The spring–neap modulation of tide is represented through the following open boundary condition:

$$\bar{u}-\bar{u}_m-\left[1-\eta_{ms}\cos\left(\frac{2\pi}{T_{ms}}t\right)\right]\bar{u}_T = \frac{\sqrt{gh}}{h}\left\{\xi-\xi_m-\left[1-\eta_{ms}\cos\left(\frac{2\pi}{T_{ms}}t\right)\right]\xi_T\right\}, \tag{19}$$

where η_{ms} is the ratio of the amplitude of S_2 to the amplitude of M_2 tide ($=0.4$) and T_{ms} is the modulation period ($=14.77$ days). For the seasonal variation in the oceanic flows, the open boundary condition is given by

$$\bar{u}-\left[1-\eta_o\cos\left(\frac{2\pi}{T_o}-\varphi\right)t\right]\bar{u}_m-\bar{u}_T = \frac{\sqrt{gh}}{h}\left\{\xi-\left[1-\eta_o\cos\left(\frac{2\pi}{T_o}-\varphi\right)t\right]\xi_m-\xi_T\right\}, \tag{20}$$

where η_o is the amplitude of the seasonal variation in the oceanic inflows and outflows (chosen here as 0.4), T_o is the modulation period ($=365$ days) and φ is the phase lag ($=60$ days). We assume that the minimum of the volume transport is located around the end of February and the modulations of inflows and outflows are in phase with each other.

Fig. 12 displays the local and cumulative transports at Section C of Fig. 1, which is defined as the southern boundary of the YS in this study, computed with the spring–neap modulation of the open boundary tide. The thin broken and solid lines indicate the local transports at spring and neap tides, respectively, while the thick broken and solid lines indicate the corresponding cumulative transports. To focus on the effects of the spring–neap modulation on the oceanic circulation rather than the tide plus oceanic circulation, the local volume transport at each grid point is calculated by subtracting the volume transport computed with tide only from the volume transport computed with tide and oceanic flows. The cumulative transports have been obtained by adding the local transports from the left to the right of Section C. We can see that the corresponding changes in the volume transports are clearly shown. The positive flux is distributed broadly over the western and

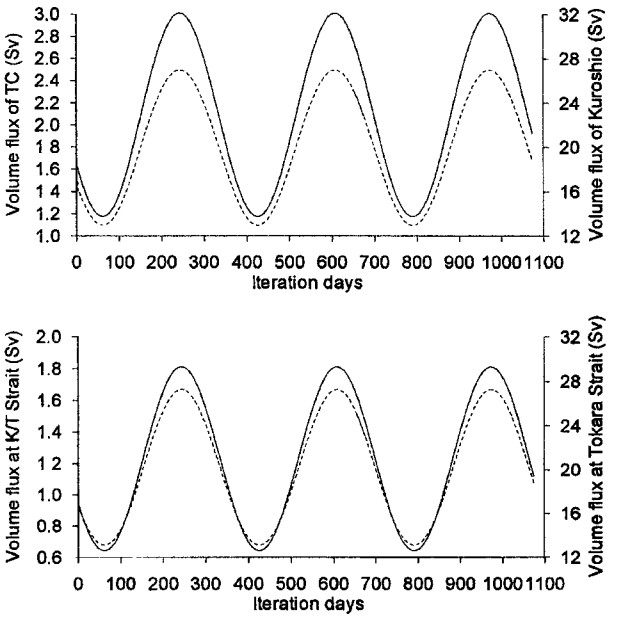

Fig. 12. Calculated volume transports along Section C in Fig. 1: local volume transports at spring (thin solid line) and neap (thin broken line), and cumulative transports at spring (thick solid line) and neap (thick broken line).

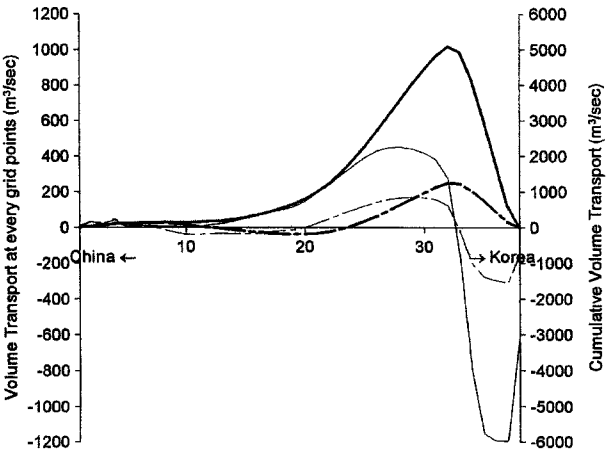

Fig. 13. Calculated seasonal variation in volume transports at inflow regions, the TC (dotted line) and the Kuroshio (solid line), and at outflow regions, Korea/Tsushima Strait (dotted line) and Tokara Strait (solid line).

central parts of the YS, giving weaker northward flows, while the negative flux occurs in narrow regions biased to the side of west coast of Korea, giving strong compensatory southward flows. It is interesting to note that the negative flux region is more biased to the east in case of neap tide. We note that the flux at the spring tide is significantly smaller than that of neap tide. This is attributed to the difference in the bottom frictional dissipations of spring and neap tides. That is, the enhanced bottom friction at the spring tide suppresses the penetration of the oceanic current into the YS.

From the results shown in Fig. 12, we see that the amount of volume exchange at neap and spring tides is about $5000\,m^3/s$ ($=0.005$ Sv) and $1000\,m^3/s$ ($=0.001$ Sv), respectively. There is, however, little data to support the result. In fact, taking into account the relatively small water movement compared with currents driven by tide and local wind in the YS and the ECS, it is hard to estimate the volume transport quantitatively at the boundary. Yang et al. (1998) have recently suggested based on a simple salt budget box model that, in oder to maintain the salinity in the YS, the volume of $2.105\,km^3/yr$ (≈ 0.066 Sv) should intrude into the YS through the boundary, which was defined as the line connecting the southwestern tip of the Korean Peninsula and the north of the mouth of the Yangtze River, and the net outgoing volume transport from the YS due to the evaporation, the precipitation and river discharges in the YS approximately amounts to $148\,km^3/yr$ (≈ 0.004 Sv). Lee et al. (1999) estimated the amount of volume transport across the boundary between the YS and the ECS, which was roughly the same as that of Yang et al. (1998), as about $2462.4\,km^3/yr$ (≈ 0.078 Sv) and the net outgoing volume transport as $121.4\,km^3/yr$ (≈ 0.004 Sv) based on the salt budget of the YS calculated with the CTD data collected during 1996–1998 and climatological data. The volume transport calculated with our model approximately amounts to 10% of that of Yang et al. (1998) and Lee et al. (1999). In this study, however, we excluded the effect of stratification and wind forcings. It is well known that the oceanic circulation in the YS is mainly driven by a strong northwesterly wind in winter time. Inclusion of wind forcings, along with the effect of spring–neap modulation, might give rise to a larger variation in the volume transport across the boundary of the southern YS.

Fig. 13 shows the time variation in the volume transports at the four openings, in detail, the shelf

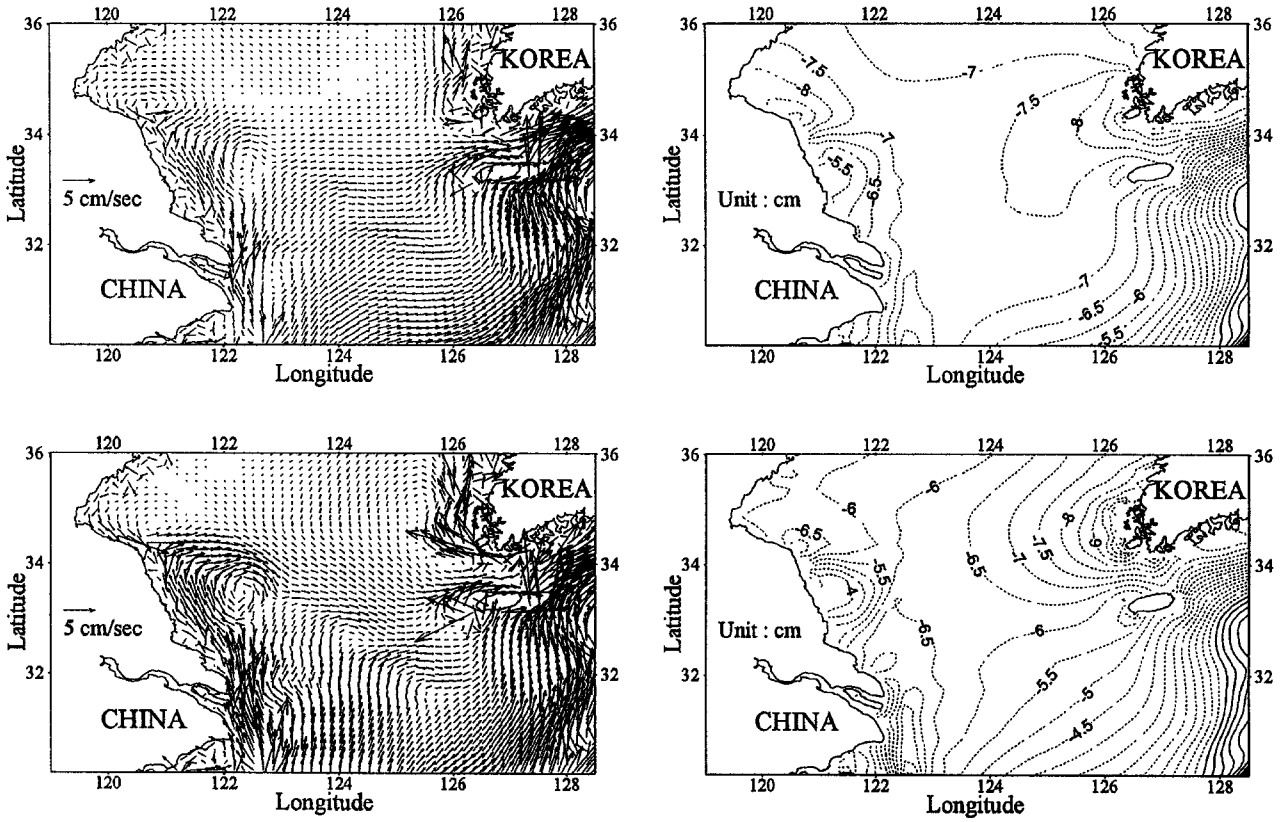

Fig. 14. Time-averaged sea surface flow and elevation fields west of Cheju Island at neap (upper) and spring (lower) tide.

break east of Taiwan and Taiwan Strait (solid and dotted lines in the upper diagram, respectively), Korea/Tsushima Strait and Tokara Strait (solid and dotted lines in the lower diagram), computed with the seasonal variation in the oceanic flows. At the inflow regions, the volume transport of the Kuroshio fluctuates from 14 to 32 Sv, while the TC varies from 1.1 to 2.5 Sv. These values are nearly identical with estimates given by Yuan et al. (1994) and Zhao and Fang (1991), respectively. As a consequence, the volume transports in the outflow regions increase: in the Korea/Tsushima Strait from 0.7 Sv in winter to 1.7 Sv in summer, while in Tokara Strait from 13 Sv in winter to 30 Sv in summer, respectively. The resultant variation in volume transport at Section C is less than 0.001 Sv (result not shown).

Fig. 14 shows the residual flow fields at the sea surface and the time-averaged sea surface elevation at the times of neap (upper) and spring (lower) tides, respectively. It is evident that both the magnitude and the direction of the residual currents differ from each other. It is generally known that the magnitude of the mean current does not change as much as the change in the input energy since the additional energy is transferred to higher frequencies as well as the mean field, and more energy is dissipated by bottom friction as well. It is noticeable that the anti-clockwise flow off the southern tip of the Korean Peninsula is much more pronounced than that of neap tide. Furthermore, it is seen that the distinctive northward flow is formed around 31°N and 124° in the case of spring tide, whereas the flows are northeastward or nearly eastward flow is formed in the case of neap tide. The enhanced bottom friction due to the strong tidal currents might drive the northward flows across the isobaths at consider-

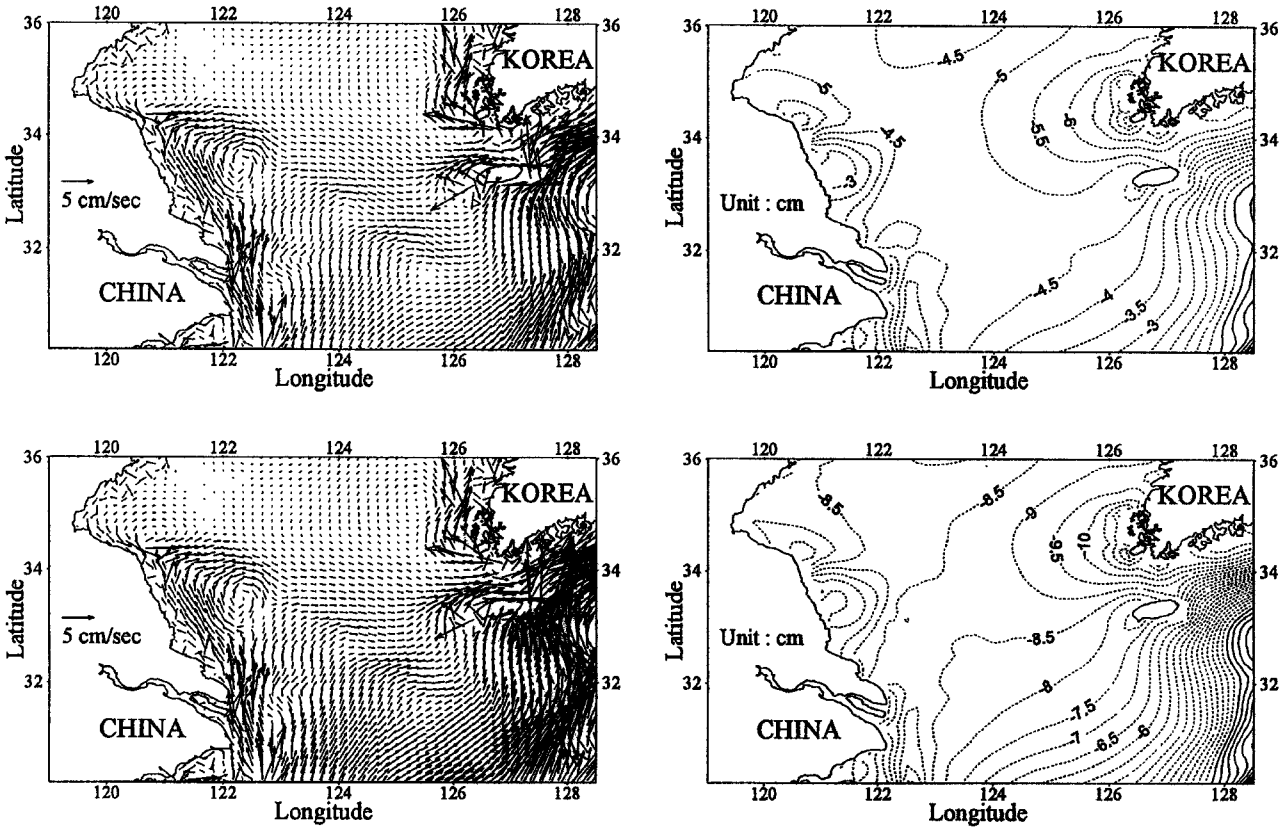

Fig. 15. Time-averaged sea surface flow and elevation fields west of Cheju Island at minimum (upper) and maximum (lower) oceanic inflows/outflows.

able angles. A similar tendency can be identified in the distributions of the time-averaged sea surface elevation. We can see that there is a distinctive difference in the distributions of sea surface elevation around the southwestern tip of the Korean Peninsula.

Fig. 15 shows the residual flow fields at the sea surface and the time-averaged sea surface elevation at the times when the volume transport of the oceanic flows reaches its minimum (upper) and maximum (lower), respectively. Some differences are noted in the magnitudes of the oceanic flows southwest of Cheju Island, but the flow patterns are quite similar to each other. Especially, the anti-clockwise flows off the southwestern tip of the Korean Peninsula are commonly shown. The horizontal gradients of sea surface elevation around the southwestern tip of the Korean Peninsula also reveal similar patterns, but the sea surface gradient becomes steeper as the volume transport of the oceanic flows reaches its maximum, especially in areas south of Cheju Island where the circulation might be strongly influenced by the oceanic flows. We conclude that the seasonal variation in the volume transport of the oceanic inflows/outflows without baroclinic effects has little effect on the exchange between the YS and the ECS.

4. Conclusion

Our major concern in this study was to confirm the previous results, that is, Exp. 4 of Lee et al. (2000) in which the effects of tidal stirring due to M_2 tide were incorporated, through the use of a

space-dependent bottom frictional coefficient defined by Hunter's (1975) formula as well as the enhanced value of the vertical eddy viscosity, taking into account the M_2 tidal current amplitudes known a priori. In this study, model experiments have been carried out by driving the motion with oceanic flows plus M_2 open boundary forcings. For that, the radiation condition used in Lee et al. (1999) has been further extended. The bottom friction has been represented by a quadratic friction law and the vertical eddy viscosity is given in a flow-related form. The stratified structure of the Kuroshio has been again approximated by introducing an empirical function of the exponential type for the representation of current profile below the main stream of Kuroshio. Prior to the model run with oceanic flows plus M_2 tide, considerable efforts have been directed to determine an optimum value of the bottom friction coefficient. The use of an empirical function expansion results in the bias of the tidal propagation and the associated flux, but to a degree which has been found to be tolerable.

The model calculation confirms the results of Exp. 4 of Lee et al. (2000), in that the bottom friction increased by the presence of strong tidal currents effectively blocks the penetration of northwestward flow into the YS known as the YSWC. The presence of small gyres complicates the circulation near the southern YS and west of Cheju Island. Northward flows of tidal nonlinearity origin, which is absent in the result of Exp. 4 of Lee et al. (2000), reach further north and then turn sharply to Cheju Strait. We could see that there are southeastward tidal residual currents west of Cheju Island, particularly along the downhill region with depths of 30–70 m. These residual currents additionally contribute to suppression of the development of the YSWC, consequently, reducing the volume flux through Section A (connecting Cheju Island and the Chinese coast) to 1.1 Sv. For the direct comparison of oceanic currents computed from Exp. 4 of Lee et al. (2000) and Calcn. 7, we have approximately extracted the oceanic current field from Calcn. 7 by subtracting the result of Calcn. 2 from the result of Calcn. 7. Although the result is not shown here, both results are similar to each other but there are some differences in the magnitudes and directions of current, particularly around the west of Cheju Island. Exp. 4 might underestimate slightly the bottom friction compared to Calcn. 7. We emphasize that in the absence of wind stress and baroclinic effects, our results, that is, Calcn. 7 in this study and Exp. 4 of Lee et al. (2000), do not give any evidence for the existence of the YSWC penetrating into the interior of the YS. The spring–neap modulation controls, to some degree, the flux of oceanic currents into the YS, whereas the seasonal change in the inflows and outflows barely affects the exchange between the YS and the ECS.

It is seen that tidal nonlinearities might be important particularly along the west coast of Korea and the Chinese coast. Unfortunately, there are no observations to compare the model results with. Long-term moorings at the positions where the presence of strong tidal residuals is predicted are very demanding (it is noted that Larsen et al. (1985) never reported the result on residuals). Furthermore, better resolution for more realistic calculation of tidal residuals and a more sophisticated model for bottom friction might be needed. Our next concern in the YS and the ECS includes the variation of the oceanic circulation under wind forcings. Model runs on this matter are underway and will be soon reported. The present model does not include the components of residual flows which may be produced by winds, density gradients and freshwater discharge. There is some progress in baroclinic modeling which incorporates the discharge from the Yangtze River and solar radiation at the sea surface. This will also be reported in the near future.

Acknowledgements

This research was funded by various projects carried out in the period of 2000–2001: 'Development of monitoring strategy for marine environmental radioactivity', 'Development of monitoring technology for the waste disposal sea area', and 'An assessment of environmental fate of contaminants' under contract with the Ministry of Science and Technology of Korea.

References

Backhaus, J., 1979. First results of a three-dimensional model on the hydrodynamics in the German Bight. In: Nihoul, J C.J. (Ed.), Marine Forecasting, Predictability and Modelling in Ocean Hydrodynamics. Elsevier, Amsterdam, pp. 333–349.

Beardsley, R.C., Limeburner, R., Hu, D., Le, K., Cannon, G.A., Pashinski, D.J., 1983. Structure of Changjiang River plume in the East China Sea during June 1980. In: International Symposium on Sedimentation on the Continental Shelf, with special reference to the East China Sea. China Ocean Press, China, pp. 243–260.

Beardsley, R.C., Limeburner, R., Kim, K., Candela, J., 1992. Lagrangian flow observations in the East China, Yellow and Japan Sea. La mer 30, 297–314.

Blain, C.A., 1997. Development of a data sampling strategy for semiclosed seas using a shallow-water model. Journal of Atmospheric and Oceanic Technology 14, 1157–1173.

Bowman, M.J., Chiswell, S.T., 1982. Numerical tidal simulation within the Hauraki Gulf, New Zealand. In: Nihoul, J.C.J. (Ed.), Hydrodynamics of Semi-enclosed Seas. Elsevier, Amsterdam, pp. 349–384.

Candela, J., Beardsley, R.C., Limeburner, R., 1992. Separation of tidal and subtidal currents in ship-mounted Acoustic Doppler Current Profiler Observations. Journal of Geophysical Research 97, 769–788.

Chen, C., Beardsley, R.C., Limeburner, R., 1992. The structure of the Kuroshio southwest of Kyushu: velocity, transport and potential vorticity field. Deep Sea Research I 39, 245–268.

Choi, B.H., 1980. A tidal model of the Yellow Sea and the eastern China Sea. Korea Ocean Research and Development Institute Report 80-20, 72pp.

Davies, A.M., 1977a. The numerical solution of the three-dimensional hydrodynamic equations using a B-spline representation of the vertical current profile. In: Nihoul, J.C.J. (Ed.), Bottom Turbulence, Proceedings of the Eighth Liege Colloquium on Ocean Hydrodynamics, Elsevier Oceanography Series 19, pp. 1–25.

Davies, A.M., 1977b. Three-dimensional model with depth-varying eddy viscosity. In: Nihoul, J.C.J. (Ed.), Bottom Turbulence, Proceedings of the Eighth Liege Colloquium on Ocean Hydrodynamics, Elsevier Oceanography Series 19, pp. 27–48.

Davies, A.M., 1978. The use of the Galerkin method with a basis set of B-spline for the solution of one-dimensional primitive equation. Journal of Comparative Physics 27, 123–137.

Davies, A.M., Aldridge, J.N., 1993. A numerical model study of parameters influencing tidal currents in the Irish Sea. Journal of Geophysical Research 98, 7049–7067.

Davies, A.M., Kwong, S.C.M., Flather, R.A., 1997. Formulation of a variable-function three-dimensional model, with applications to the M_2 and M_4 tide on the North-West European continental shelf. Continental Shelf Research 17, 165–204.

Fang, G., 1986. Tide and tidal current chart for the marginal seas adjacent to China. Chinese Journal of Oceanology and Limnology 4, 1–16.

Flather, R.A., 1976. A tidal model of the north west European Continental Shelf. Memories de la Societe Royale des Science de Liege 10, 141–164.

Guo, X., Yanagi, T., 1998. Three-dimensional structure of tidal current in the East China Sea and the Yellow Sea. Journal of Oceanography 54, 651–668.

Harkema, R., Hsueh, Y., 1987. A comparison of moored current data in the Eastern Yellow Sea, January–April 1986. Technical Report CMF-87.01. Department of Oceanography, Florida State University, Tallahassee.

Huh, H.T., et al., 1985. A study on the Atlas of marine resources in the adjacent seas to Korea, Yellow Sea. MOST Report BSPE00055-86-7A, 523pp. (in Korean).

Hunter, J.R., 1975. A note on quadratic friction in the presence of tides. Estuarine and Coastal Marine Science 3, 473–475.

Ichikawa, H., Beardsley, R.C., 1993. Temporal and spatial variability of volume transport of the Kuroshio in the East China Sea. Deep-Sea Research 40, 583–605.

Japan Oceanographic Data Center, 1978. Marine Environmental Atlas—Northwestern Pacific Ocean II, p. 157.

Kaneko, A., Koterayama, W., Honji, H., Mizuno, S., Kawatate, K., Gordon, R.L., 1990. Cross-stream survey of the upper 400 m of the Kuroshio by an ADCP on a towed fish. Deep Sea Research 37, 875–889.

Kaneko, A., Byun, S.K., Chang, S.D., Takahashi, M., 1991. An observation of sectional velocity structures and transport of the Tsushima Current across the Korea Strait. In: Takano, K. (Ed.), Oceanography of Asian Marginal Seas, Elsevier Oceanography Series 54, Amsterdam, pp. 179–195.

Kang, S.K., Lee, S.R., Lie, H.J., 1998. Fine grid tidal modeling of the Yellow and East China Seas. Continental Shelf Research 18, 739–772.

Larsen, L.H., Cannon, G.A., Choi, B.H., 1985. East China Sea tide currents. Continental Shelf Research 4, 77–103.

Lee, H.J., Jung, K.T., Foreman, M.G.G., Chung, J.Y., 2000. A three-dimensional mixed finite-difference Galerkin function model for the oceanic circulation in the Yellow and the East China Sea. Continental Shelf Research 20, 863–895.

Lee, J.C., Jung, K.T., 1996. Computation of M_2 tide for the Yellow Sea and the East China Sea using data assimilation. Ocean Research 18, 13–24 (in Korean).

Lee, J.C., Jung, K.T., 1999. Application of eddy viscosity closure models for the M_2 tide and tidal currents in the Yellow Sea and the East China Sea. Continental Shelf Research 19, 445–475.

Lee, J.H., An, B.W., Bang, I.K., Lie, H.J., Tang, Y., 1999. Water and salt budgets for the Yellow Sea. In: Hong, G.H., Zhang, J., Chung, C.S. (Eds.), Biogeochemical Processes in the Bohai and Yellow Sea. The Dongjin Publication Association, Seoul, pp. 221–234.

Lie, H.J., Cho, C.H., 1997. Surface current fields in the eastern East China Sea. The Journal of the Korean Society of Oceanography 32, 1–7.

Nihoul, J.C.J., Runfola, Y., 1981. The residual circulation in the North Sea. In: Nihoul, J.C.J. (Ed.), Ecohydrodynamics. Elsevier, Amsterdam, pp. 219–271.

Nishida, H., 1980. Improved tidal charts for the western part of the North Pacific Ocean. Reports of Hydrographic Researches 15, 55–70.

Sternberg, R.W., Larsen, L.H., Yutian, M., 1983. Near-bottom conditions and associated sediment transport on the East China Sea continental shelf. In: International Symposium on Sedimentation on the Continental Shelf, with special reference to the East China Sea. China Ocean Press, China, pp 486–498.

Wolf, J., 1987. A 3-D model of the Severn Estuary. In: Nihoul, J.C.J., Jamart, B.M. (Eds.), Ecohydrodynamics. Elsevier, Amsterdam, pp. 609–624.

Woodruff, S.D., Slutz, R.J., Jenne, R.L., Steurer, P.M., 1987. A comprehensive ocean-atmosphere data set. Bulletin of American Meteorological Society 68, 1239–1250.

Yanagi, T., Takahashi, S., 1993. Seasonal variation of circulations in the East China Sea and the Yellow Sea. Journal of Oceanography 49, 503–520.

Yanagi, T., Morimoto, A., Ichikawa, K., 1997. Seasonal variation in surface circulation of the East China Sea and the Yellow Sea derived from satellite altimetric data. Continental Shelf Research 17, 655–664.

Yang, D.B., et al., 1998. On the material balance and biogeochemical cycle of the Yellow Sea. MOST 97-LO-01-03-A-03, 437pp. (in Korean).

Yi, S.U., 1966. Seasonal and secular variations of the water volume transport across the Korea Strait. The Journal of the Korean Society of Oceanography 1, 7–13.

Yuan, Y., Pan, Z., Kaneko, I., Endo, M., 1994. Variability of the Kuroshio in the East China Sea and the currents east of the Ryukyu Islands. In: Proceedings of China–Japan Joint Symposium of the Cooperative Research on the Kuroshio. China Ocean Press, Beijing, China, pp. 121–144.

Zhao, B., Fang, G., 1991. Estimation of water volume transports through the main straits of the East China Sea. Acta Oceanologica Sinica 10, 1–13.